Examination of the changes in spatial structure of the turbulent boundary layer under wave forcing using Proper Orthogonal Decomposition

Maius Wong

A dissertation
submitted in partial fulfillment of the
requirements for the degree of

MASTER OF SCIENCE IN AERONAUTICS & ASTRONAUTICS

University of Washington

2018

Reading Committee:

Owen J. H. Williams, Chair

Mitsuru Kurosaka

Program Authorized to Offer Degree:
Aeronautics & Astronautics

University of Washington

Abstract

Examination of the changes in spatial structure of the turbulent boundary layer under wave forcing using Proper Orthogonal Decomposition

Maius Wong

Chair of the Supervisory Committee:
Research Assistant Professor Owen J. H. Williams
Aeronautics & Astronautics

The interaction between bottom turbulent boundary layers and surface waves has previously been characterized using point-wise, statistical methods suggesting significant non-linear changes to turbulent boundary layer structure. To examine changes to these structures, a detailed set of experiments were conducted using a combination of wave-height sensors and particle image velocimetry (PIV) to examine the bottom turbulent boundary layer under quasi-sinusoidal waves of differing amplitude. Spatial structures were examined using proper orthogonal decomposition (POD), which has been demonstrated to reveal near-wall attached structures that have been seen to contribute to the majority of negative turbulent shear stress and positive turbulent kinetic energy production in conventional boundary layer flows. Through an examination of streamwise and wall-normal modes it is demonstrated that POD is able to reveal these structures in the present dataset despite the presence of the free surface and high freestream turbulence of the current facility. Under surface wave forcing, the streamwise structures were seen to exhibit a higher inclination than in the unperturbed boundary layer, and wall-normal modes that are detached from the wall. In addition, there is loss of anti-correlation between streamwise and wall-normal modes resulting in stronger positive and weaker negative shear stress events that are clustered further from the wall suggesting significant disruption to turbulent production mechanisms.

TABLE OF CONTENTS

LIST OF FIGURES

Figure Number Page

LIST OF TABLES

Table Number Page

NOMENCLATURE

a: Peak-peak amplitude of the surface waves

C_f: Coefficient of friction at the plate boundary

H: Channel depth (from free surface to boundary)

k: Turbulent kinetic energy

u: Streamwise velocity

u_τ: Friction velocity

v: Wall-normal velocity

δ_0: Boundary layer thickness as calculated for the wave-free case

η: Wave height above the free surface

λ: Surface wave wavelength

$\langle \cdot \rangle$: Ensemble-averaged quantity

$(\cdot)'$: Fluctuating quantity

$(\tilde{\cdot})$: Periodic quantity

$(\bar{\cdot})$: Mean quantity

$(\cdot)^+$: Denotes inner co-ordinates

$(\cdot)_\infty$: Denotes free-stream values

ACKNOWLEDGMENTS

First and foremost, I would like to thank my advisor, Professor Owen Williams. Over the past year and a half, I was able to get back to my roots in experimental fluid mechanics, and had the chance to look at the turbulent boundary layer, one of the fields' most challenging, unsolved problems to date. All of which would have been impossible without his help and guidance through this degree. I would like to thank Professor Mitsuru Kurosaka for providing valuable feedback as part of my thesis committee. As a TA for one of his classes for this final quarter, I would like to thank him for his kindness and understanding as well, in providing me with extra time to complete my TA duties in order to finish my dissertation.

I would also like to express my gratitude to Professor Andy Jessup, whose expertise on the workings of the University of Washington's Air-Sea Interaction Research Facility were invaluable for getting this experiment running. I would also like to thank Professor Brian Polagye for working with us at Harris Hydraulics Laboratory, allowing us to complete our experiments in a timely manner.

I would like to thank the Aeronautics & Astronautics department for providing me with the chance of conducting this research. As the son of two University of Washington graduates, I was humbled and grateful to have received a generous funding package, allowing me to continue the family tradition. Finally, and in that spirit, I would like to thank my mom and dad. Thirty years ago, almost to the day, you walked across the stage and received your Master's degrees from this institution. Through your continued belief in me, through French immersion, high school, college in a city we'd never heard of, and bringing it full circle back to the Pacific Northwest, I am proud to say that I will be doing the same this year.

DEDICATION

To mom and dad

Chapter 1

INTRODUCTION

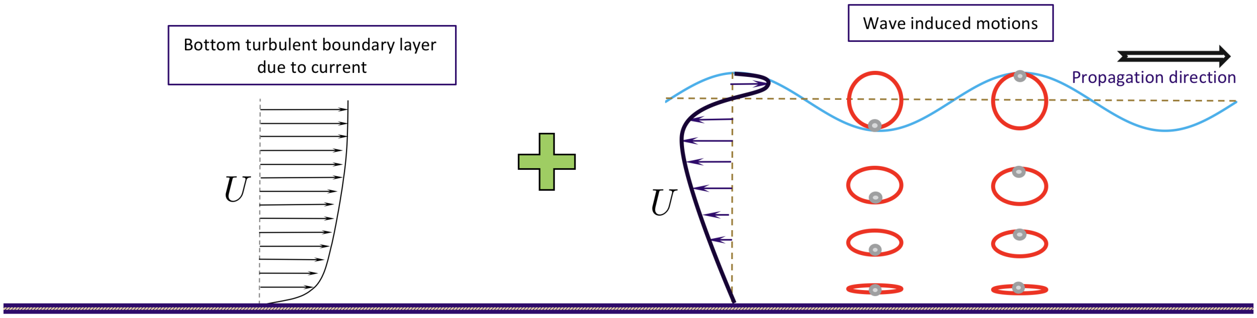

Figure 1.1: Schematic of the surface wave-turbulent boundary layer interaction

The interaction between a surface wave and an underlying turbulent boundary layer is an interaction commonly seen in nature. This type of interaction, common to marine estuarine environments, can significantly affect the transport of sediment and the spread of algal blooms. An example is the red tide, which has the potential to significantly harm the fishing economies of cities such as Seattle and San Francisco. In engineering, a better understanding of this coupled interaction has the potential to provide key insights into achieving better power extraction from tidal currents, and to better understand the drag characteristics of subsurface vehicles.

Various studies over the past three decades have attempted to characterize the interaction using point-wise statistical methods. Klopman (1994, Figure 1.2 left), for example, discovered that the shape of the mean velocity profile changes substantially when the turbulent boundary layer is subjected to following or opposing waves. Kemp & Simons (1982, Figure 1.2 right) showed that a linear superposition of both the mean velocity profiles observed from

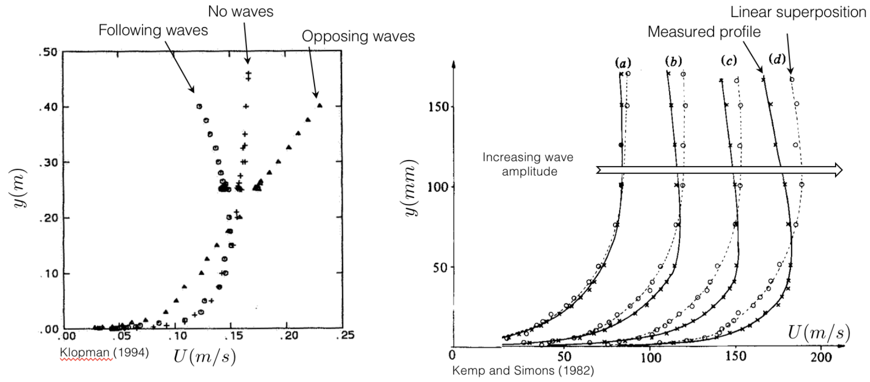

Figure 1.2: (left) Experiment conducted by Klopman (1994) showing the effect of following and opposing waves on the mean velocity profile, and (right) mean profiles of current-following waves conducted by Kemp & Simons (1982) and their linear superpositions. Both results suggest changes to the underlying turbulent boundary layer structure, but such a change cannot be clearly identified using point-wise methods.

a current and from wave forcing, measured separately, does not predict the wave-turbulent boundary interaction, suggesting that the wave-turbulent boundary layer interaction is non-linear. In this experiment, we aim to observe changes in the spatial structure in an attempt to understand the non-linear interactions identified in previous literature. In other words, we aim to understand *how* the turbulent boundary layer structure changes when subjected to surface wave forcing.

To this end, we employ proper orthogonal decomposition (Sirovich 1987; Holmes et. al. 1998). Described further in Chapter 5, the method provides a set of linear, orthogonal, spatial modes weighted by their contributions to turbulent kinetic energy k. When the turbulent boundary layer is decomposed using POD, the result is a set of wall-attached, inclined modes which are anti-correlated in streamwise and wall-normal velocity. These modes, reminiscent of hairpin packets, result in negative shear stresses near the wall. In the boundary layer, where the mean velocity gradient is positive, these negative shear stresses are a source of turbulent kinetic energy production. Recently, these hairpin packets were determined to be self-similar (Hellström 2016).

In this experiment, data from the Washington Air-Sea Interaction Flume (WASIRF) is collected using particle image velocimetry (PIV) and in five sets: a current-only case (C), a weak wave case (W1), a wave case (W2) and a combination of waves and current (W1C and W2C). This data is then analyzed using two methods: first, the traditional, statistical methods are employed and compared with previous experiments, and second, proper orthogonal decomposition is performed to examine the spatial structure of the flow. It will be shown that the results from statistical methods agree with previous experiments to an extent, but the presence of a surface wave directly results in significant structural changes to the attached modes.

Chapter 2

EXPERIMENTAL SET-UP

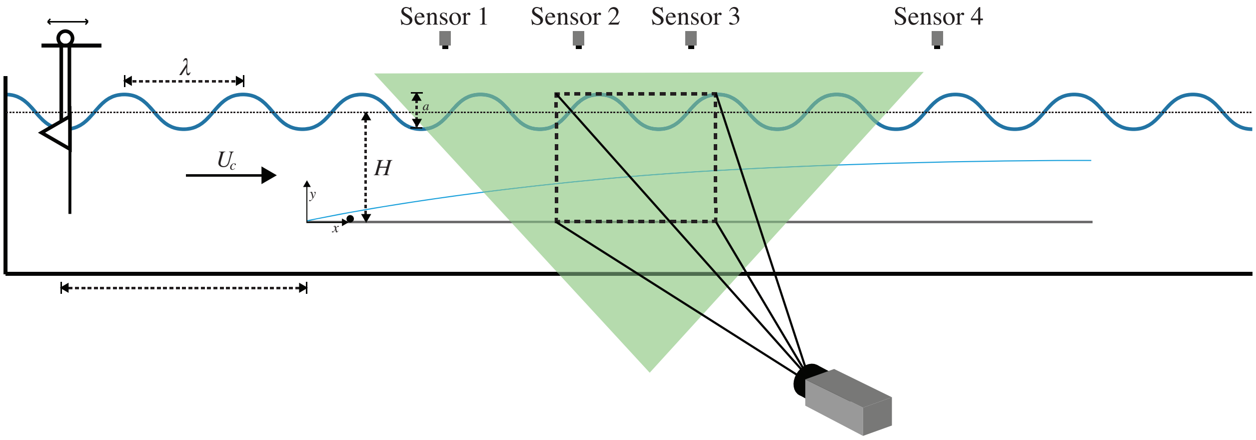

Figure 2.1: Diagram of the experimental set-up, where H is the depth of the plate below the free surface, λ is the wavelength, and a is the peak-to-peak amplitude of the wave.

To generate a turbulent boundary layer for analysis, we use the water channel known as the University of Washington Air-Sea Interaction Facility (WASIRF). This channel, previously installed at NASA Wallops, is described in detail in Huang & Long (1980). The channel has a rectangular cross-section of 0.91 m in width and a maximum depth of 0.76 m. At maximum water depth, the channel is capable of producing a free-stream velocity of 0.38 m/s. The channel test section has since been shortened from 60 to 40 ft, and a mechanical wave generator has been installed upstream of the test section. Inside the channel, a smooth, half-inch thick plexiglass plate of about 600 cm is placed at a depth $H = 23$ cm below the free surface, on which the turbulent boundary layer is developed. To assist in turbulent boundary layer development, a trip wire with a circular, 1.6 mm cross-section is placed approximately 0.3 m from the leading edge of the plate. Turbulent boundary layer generation, wave generation, and data capture are discussed in the following sections.

2.1 Turbulent Boundary Layer Generation

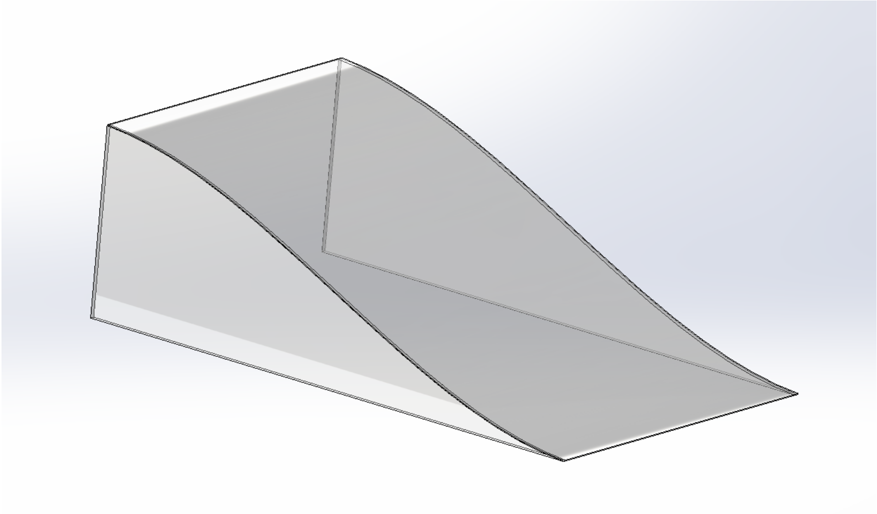

Figure 2.2: Schematic of the leading edge ramp.

The channel current is driven by a variable-frequency drive pump which is controlled by a remote panel and has a maximum operating frequency of 20 Hz. At this frequency and when filled to maximum depth, the channel is capable of producing a free-stream velocity of 0.38 m/s. In this configuration, the freestream turbulence is roughly $5\%u_\infty$, which is relatively high. In an attempt to reduce the free-stream turbulence, a ramp was installed in front of the plate such that the flow is contracted, and is directed above the smooth plexiglass plate. The ramp profile was determined using a third-order polynomial fit, with first and second derivatives at the boundary equal to zero. A rendering of this ramp is shown in Figure 2.2. The ramp has a streamwise length of 152 cm, a spanwise width of 86 cm (roughly the width of the tunnel), and a height of 51 cm, which matches the height of the smooth plate above the channel flow. The effect of the ramp on freestream turbulence was minor, but the addition resulted in a much higher free-stream velocity of 0.9 m/s over the top of the plate. In this configuration with the ramp installed, the Reynolds number $\mathrm{Re}_\tau =$ is 2700.

Parameter	Value
δ_o	8.68 cm
$u_{\tau,o}$	0.033 m/s
C_f	0.0034
u_∞	0.9 m/s
$\mathrm{Re}_{\tau,o}$	2700
f_{wave}	1.5 Hz

Table 2.1: Test section location boundary layer conditions.

The friction velocity u_τ for the current-only case C was determined by the Clauser chart method, where the velocity profile is matched to the Law of the Wall, using Von Kármán constant $\kappa = 0.41$ and offset $C = 5.1$. Since u_τ has the potential to change when the turbulent boundary layer is subjected to wave forcing, we redefine this quantity as $u_{\tau,o}$ and we use it as a normalizing parameter for inner-coordinate quantities such as y^+ and u^+. The same reasoning is used to define the boundary layer thickness as δ_o, and the friction Reynolds number as $\mathrm{Re}_{\tau,o}$

Previous experiments in this channel showed that the velocity profile deviates below the Law of the Wall in the wake region. This may be due to an acceleration caused by the growth of sidewall boundary layers in the downstream areas of the test section, or it may be the velocity-dip effect due to the presence of the free surface in smooth channel flow (described in Yang 2004). To minimize the effect of side wall boundary layers, the current data was taken further upstream at 2 m from the plate leading edge. Measured at this location, without the presence of waves, the boundary layer thickness δ_o is determined to be 8.68 cm. Additional boundary layer parameters at the test location are shown in Table 2.1.

2.2 Surface Wave Generation

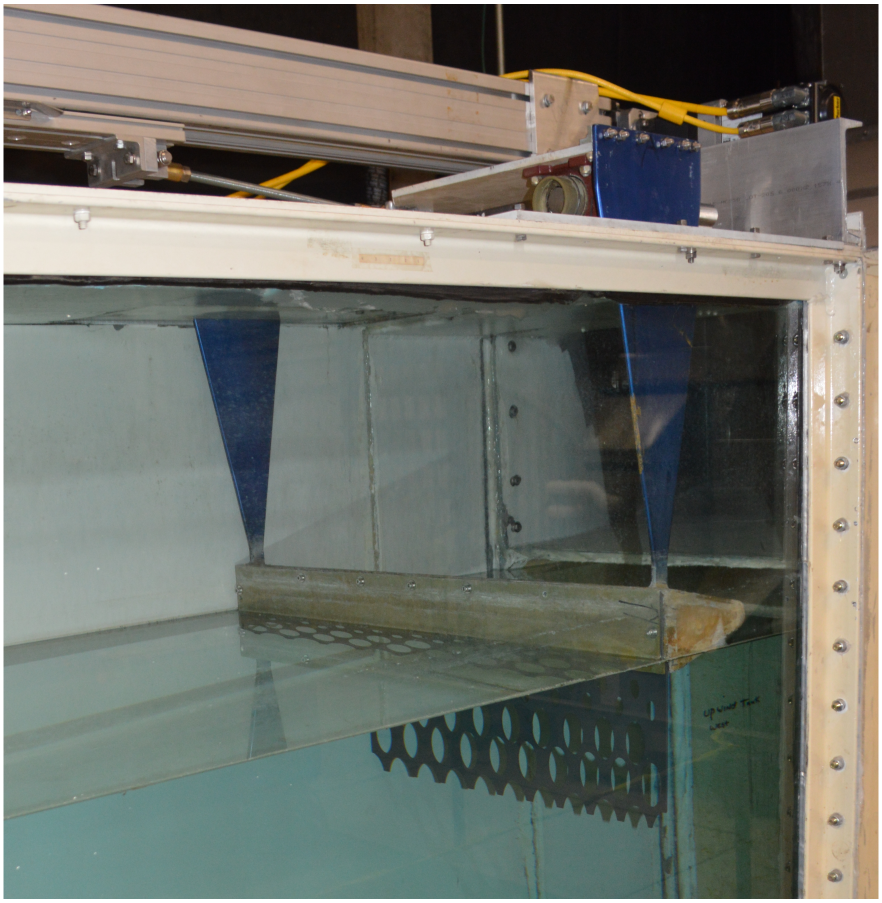

Figure 2.3: Photo depicting the wave generation system.

The wave generation system is shown in Figure 2.3. The motor, connected to a rail attached to the paddle, generated sinusoidal motions with its position driven by a Stanford Research Systems DS335 signal generator. The amplitude of the sinusoidal motions generated by the motor is proportional to the voltage amplitude from the signal generator, and is therefore the sole method of adjusting the surface wave amplitudes in the channel. Attached to the top of the paddle is a cylinder of triangular cross-section pointing upstream, ensuring that wave motions are predominantly propagated downstream. The paddle itself is a perforated acrylic sheet, with porosity increasing geometrically with depth. The result is a wave which, in the absence of current, produces an induced streamwise velocity profile which is approximate to what is predicted by linear wave theory in deep water.

To measure the wave heights generated by the paddle, four OMEGA LVU32 sensors are placed at locations 1.14, 1.55, 1.72, and 3.47 m downstream from the leading edge of the plate. These sensors are labeled 1, 2, 3, and 4, respectively. Sensors 2 and 3 are placed such that the wave speed and wavelength λ could be calculated based on a phase shift observation between the two sensors. Data was collected at 50 Hz, well above the Nyquist limit for the surface waves. The phase average of this data is calculated, and the maximum and minimum of the phase average are recorded. The result is the peak-to-peak amplitude of the wave.

2.3 Particle Image Velocimetry

2-D, 2-component PIV was used to examine the spatial structure of the bottom boundary layer. Image pairs were captured in the streamwise/wall-normal plane ($x-y$ plane in Figure 2.1). Image pairs are acquired at a rate of 6 Hz, ensuring that four frames are captured for each 1.5 Hz wave cycle. This allows for the streamwise and wall-normal wave-induced extrema to be captured. Data was collected for five different cases: a wave-free case involving only the current (denoted as C), two wave cases; one weaker, one stronger (denoted as W1 and W2 respectively), and combinations of the two (denoted W1C and W2C). Depending on the case, the interframe time (the time between capturing image pairs) is varied between 3 ms and 40 ms such that the mean particle travel distance between frames is less than half of the correlation window size. This is needed to ensure correlation between the image pairs in a frame and with adequate resolution when processing the images into vector fields.

A diagram of the PIV set-up is shown in Figure 2.1. Image pairs were collected using a 1280 px × 1024 px Mikotron EoSens camera, and particles were illuminated using a 200 mJ pulsed Nd:YAG laser mounted adjacent to and level with the channel floor. This laser, pointed normal to the streamwise/wall-normal plane, directed a laser sheet parallel to and under the plate, and was redirected to the streamwise/wall-normal plane by a 45° mirror

Figure 2.4: Sample frame showing the laser sheet diffraction, in which there is a significant drop in particle illumination. This region has been excluded from all analyses.

mounted underneath the smooth plate. Laser sheet alignment was meticulously checked to ensure that the laser sheet was parallel to the streamwise direction of the flow in order to prevent out-of-plane PIV artifacts.

Image pairs were processed into streamwise and wall-normal velocity fields by a multi-pass correlation algorithm as implemented in PIVlab (Thielicke & Stamhuis 2014). Three passes, using decreasing window sizes of 128 px × 128 px, 64 px × 64 px, and 32px × 32 px, were used. This method results in vector spacing of 85 wall units, and as a result, smaller-scale features are filtered. This is, however, adequate for this experiment because we are mainly interested in the large-scale structures in turbulent flow. These large-scale structures contain a substantial amount of kinetic energy, and it is therefore only necessary to converge the lower-order modes. Nevertheless, 20,000 frames are captured for each case to ensure sufficient modal convergence.

Vector validation is carried out using a normalized median filter, also implemented in PIVlab (Westerweel & Scarano 2005). The median filter is adjusted for each case such that the filter removes obviously erroneous vectors. During the data capture, several air bubbles were trapped underneath the smooth plate, causing diffraction in the laser sheet. This effect is shown in Figure 2.4. Particle illumination is diminished in a clear band and vector correlation is severely affected. To minimize the effect of this region, any vectors in the region outlined in red in Figure 2.4 are not considered. The vector rejection rate is 2-3% for all cases, including the bubble diffraction effects.

Chapter 3

SURFACE WAVES

Prior to the selection of the final wave conditions, tests of varying wave amplitudes in various current strengths were conducted in order to determine the possible range of paddle amplitudes and frequencies that produced sinusoidal waves. It was quickly revealed that the wave generator motor travel and its available power limited both the possible wave amplitudes and wavelengths. The addition of a current significantly increases the wavelength and reduces wave amplitude. It was therefore decided to obtain two cases of similar wave amplitude and frequency, regardless of wavelength. Additional complications arose in the identification of an appropriate wave frequency. At wave frequencies $f < 1.5$ Hz, the propagating waves were affected by interference from reflecting waves, resulting in surface waves that were incoherent. Additionally, frequencies $f > 2.0$ Hz were impossible to achieve given motor power limitations. Thus, the wave frequency was set at $f = 1.5$ Hz for all wave cases, and wave strength is varied based on a changing wave amplitude a.

Two wave amplitudes were identified in both current-free and current-forced cases. The weaker of the two amplitudes is denoted by W1, and the stronger is denoted by W2. Current-forced cases are denoted by C. Table 3.1 shows the experimental test cases and their relevant parameters. The wave heights for the different test cases were chosen such that they are roughly equal in both current-free and current-forced cases. Interference and other three-dimensional effects caused some variation (±5-10%) over the course of each experimental test case, but the phase-averaged amplitudes in similar cases with and without current (W1 & W1C, W2 & W2C) are roughly equal.

Case Name	Description	Amplitude (a, cm)	Current (u_∞, m/s)	Wavelength (λ, cm)
C	No waves, current	0	0.9	N/A
W1	Weak waves, no current	0.96	0	59.35
W2	Strong waves, no current	2.33	0	57.04
W1C	Weak waves, current	1.09	0.9	223.85
W2C	Strong waves, current	2.16	0.9	185.44

Table 3.1: Listing of experimental cases, their parameters and symbols used throughout this experiment.

3.1 Mean Induced Wave Velocity Depth Profiles

Figure 3.2 and 3.3 show the mean wave profiles for the wave-only cases. For simplicity, four wave profiles are shown: two representing the wave extrema, and two representing the crossover point between positive and negative wave-induced velocities. The waves follow an exponential profile, which appears similar in shape to linear wave theory in the short wave limit. Linear wave theory provides a reasonable model to compare with, and is widely used in engineering applications (Dean & Dalrymple 1984). When the waves are comparatively short (on the order of the surface height), linear wave theory predicts that induced streamwise velocity profiles follow an exponential curve, such that

$$\tilde{u} \sim e^{cz} \cos(\omega t)$$

where c is an undetermined constant, ω is the angular frequency, and z is the wall-normal distance from the boundary. In other words, the profile is exponential. Figure 3.1 shows the maximum induced wave profile along with an exponential profile.

When exposed to a current, we notice that the induced velocity profiles appear to match closer with linear wave theory in the long wave limit. The long wave limit limit, when $\lambda \gg H$, predicts that the wave-induced velocity profile is

$$\tilde{u} \sim c \cos \omega t$$

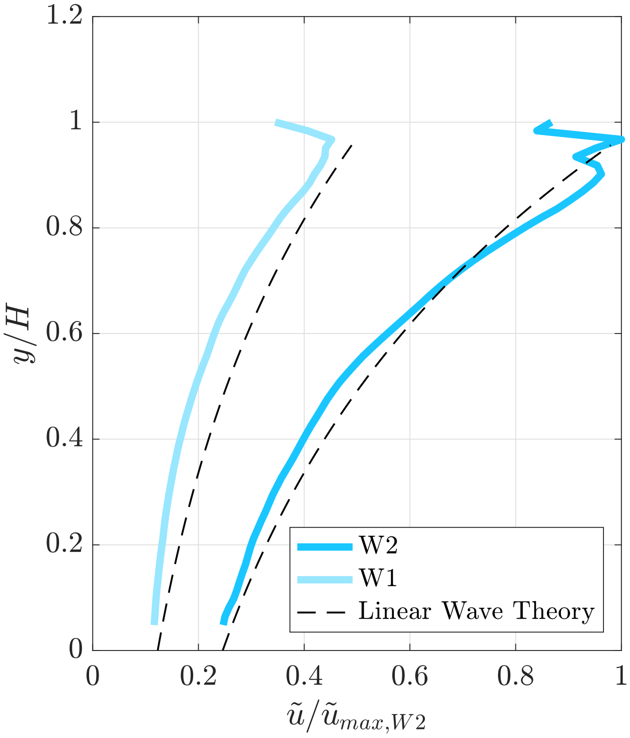

Figure 3.1: Maximum induced streamwise wave velocities from both the strong (W2) and weak (W1) wave in the absence of a current. The observed wave profiles approximately match those predicted by linear wave theory.

in other words, the velocity profile is approximately constant along the entire depth profile. We observe this change in Figures 3.4 and 3.5.

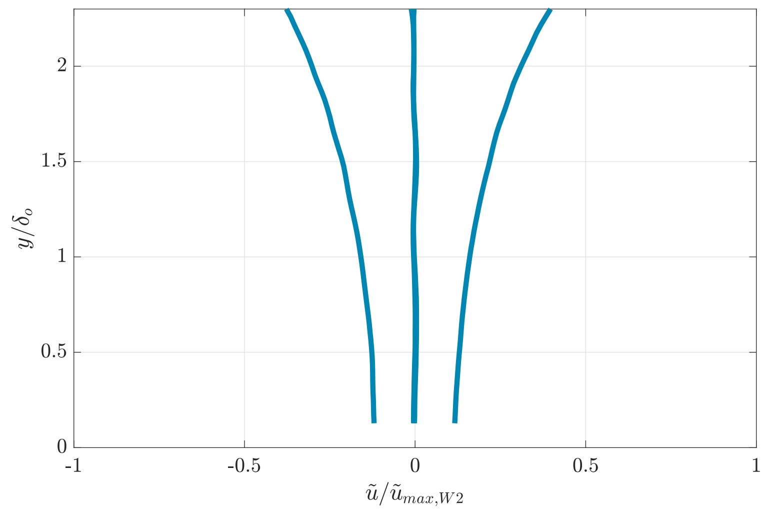

Figure 3.2: Wave profiles for case W1. Four wave profiles are plotted; two, representing the maximum and minimum induced velocities, and the other two representing the crossover between positive and negative induced velocities.

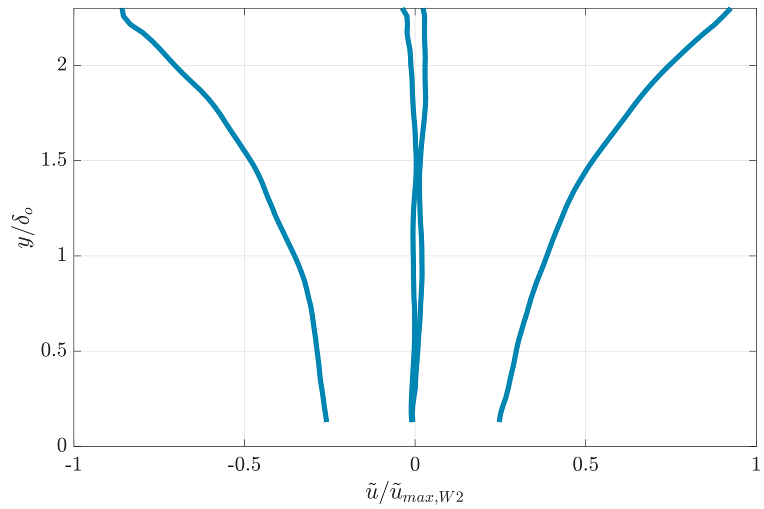

Figure 3.3: Wave profiles for case W2. Four wave profiles are plotted; two, representing the maximum and minimum induced velocities, and the other two representing the crossover between positive and negative induced velocities.

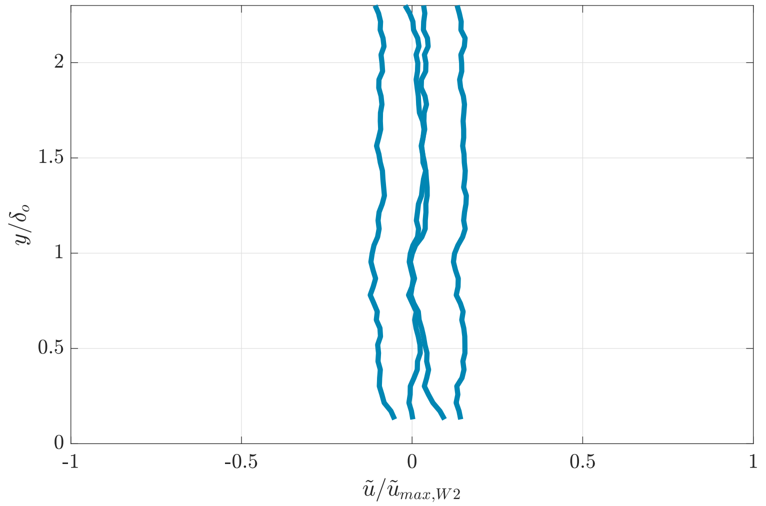

Figure 3.4: Wave profiles for case W1C. Four wave profiles are plotted; two, representing the maximum and minimum induced velocities, and the other two representing the crossover between positive and negative induced velocities.

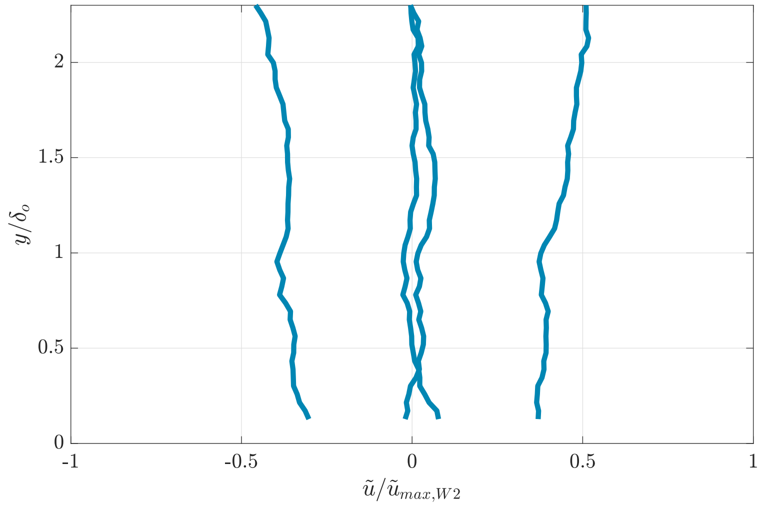

Figure 3.5: Wave profiles for case W2C. Four wave profiles are plotted; two, representing the maximum and minimum induced velocities, and the other two representing the crossover between positive and negative induced velocities.

Chapter 4

BOUNDARY LAYER STATISTICS

Statistical methods in the wave-boundary layer have typically been performed on the resulting triple decomposition (Hussain & Reynolds, 1970). This method decomposes each frame into three components: a mean flow component $\bar{u}$, a periodic component $\tilde{u}$, and a fluctuating component u'. Mathematically, each streamwise and wall-normal velocity frame can be constructed as

$$u(\mathbf{x}, t) = \bar{u}(\mathbf{x}, t) + \tilde{u}(\mathbf{x}, t) + u'(\mathbf{x}, t)$$

The mean component $\bar{u}$ is the averaged quantity at each wall-normal position. This is done by computing the average both in each spanwise location in each frame, and across all frames. The result is the mean velocity profile $\bar{u}$ which is shown for the various cases in Figure 4.1 and will be discussed later in this chapter. The periodic component $\tilde{u}$ is calculated by point-averaging each frame of identical phase, and subtracting the mean flow $\bar{u}$ from the result. Since four wave phases were captured, the result is four sets of $\tilde{u}$ spatial fields which correspond to the four phases. In each one of these frames, each streamwise location in this spatial field can be mapped to a specific phase. Finally, u' is calculated by subtracting the mean velocity $\bar{u}$ and the appropriate fluctuating velocity $\tilde{u}$ from each frame. These frames of instantaneous velocity fluctuation can then be averaged in the streamwise direction for all frames to obtain wall-normal statistical profiles of the turbulence. Likewise, the same can be computed for the wall-normal fluctuations.

4.1 Mean Velocity Profile

The mean velocity profiles in outer co-ordinates are shown in Figure 4.1. In outer co-ordinates, we note an increase in mean velocity gradient near the wall, as well as substantial changes to curvature in the wake region of the flow. These changes were identified previously in Kemp & Simons (1982) and in Klopman (1994). Kemp & Simons (1982) also identified areas of reversed velocity gradient in the wake region, which is shown in our experiment for $y/\delta_o > 2.5$. We hypothesize that this characteristic appears in waves stronger than what are used in this experiment.

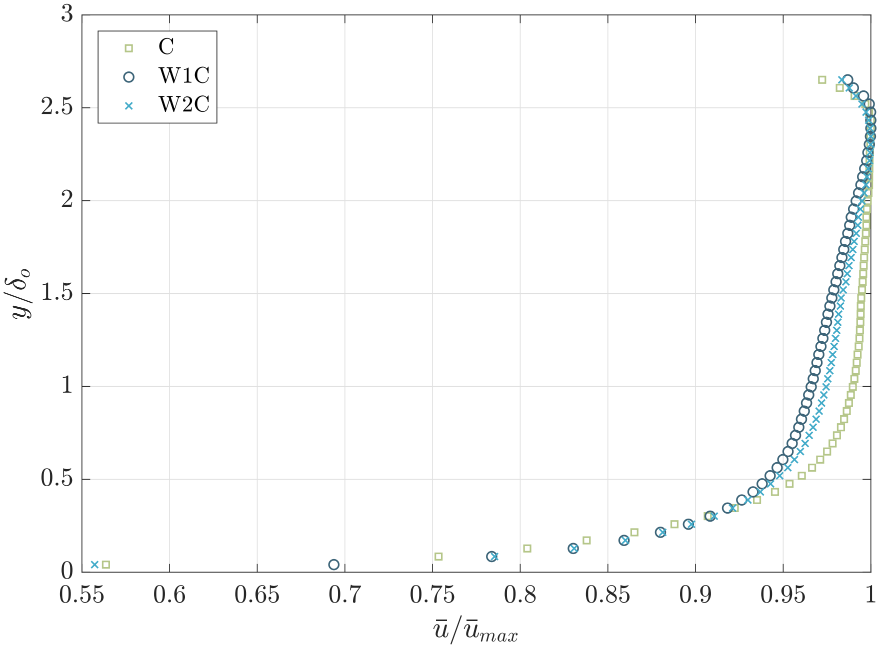

Figure 4.1: Mean profiles plotted in outer co-ordinates. Changes in mean curvature due to the presence of waves are evident, such as increased mean shear at the boundary. These results are consistent results from Klopman (1994) and Kemp & Simons (1982).

The same velocity profiles plotted in semi-log inner co-ordinates are shown in Figure 4.2, where $y^+ = yu_{\tau,o}/\nu$ and $\bar{u}^+ = \bar{u}/u_{\tau,o}$. The friction velocity $u_{\tau,o}$, the friction velocity from the current-only case C, is used as the friction velocity in all three cases and its calculation is described in Chapter 2.1. In all three of the cases, we note a deviation below the log law in the wake region of the flow. This is an odd phenomenon, as the velocity profiles are expected to deviate above the log law in the outer region in a conventional boundary layer.

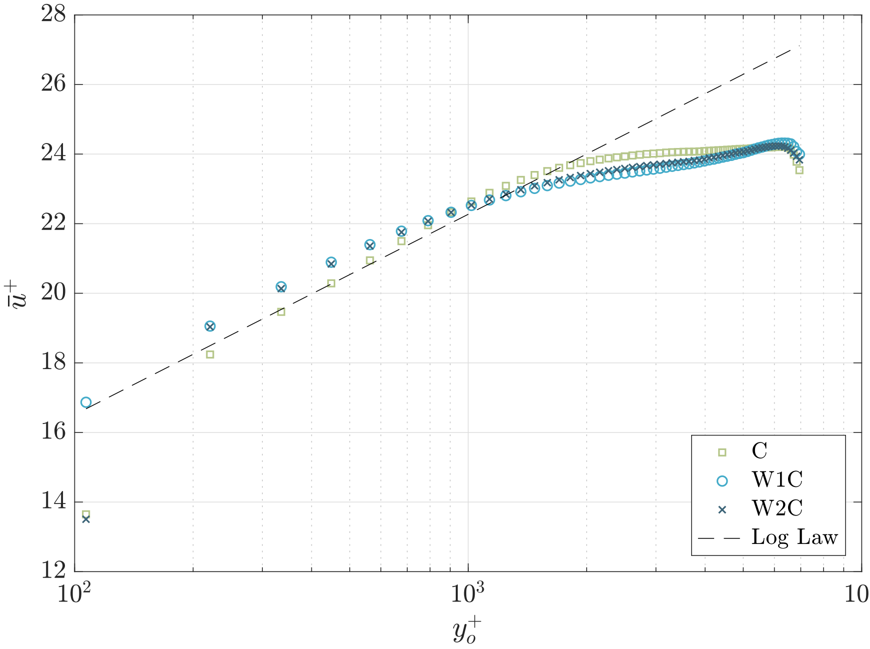

Figure 4.2: Mean profiles of C, W1C, and W2C plotted in semi-log inner co-ordinates. Two characteristics are of note: first, both mean profiles of the wave-current cases (W1C and W2C) fall above the log law in the log layer. Second, all three profiles deviate below the log law in the wake region. It is hypothesized that this is the result of a favorable pressure gradient, or a feature resembling the velocity-dip phenomenon characterized by Yang et. al. (2004)

We identify two possibilities which explain this. First, we consider that this velocity dip may be consistent with the influence of a free surface. This feature was described by Yang et. al. (2004), in which the velocity dips below the log law in smooth, open channel flows. Second, despite the addition of a ramp at the leading edge of the plate, we suspect that a favorable pressure gradient may still exist, which causes some acceleration in the wake region.

4.2 Velocity Fluctuations

Figures 4.3, 4.4, and 4.5 respectively show streamwise velocity fluctuation variances, wall-normal velocity fluctuation variances, and turbulent shear stress comparisons between Erm & Joubert (1991) and the current-only case C. The streamwise velocity fluctuations show good agreement with previous experiment, except that the datasets do not approach the same freestream value. The wall-normal fluctuation variances show poor agreement between each other. We believe that the poor agreement between the wall-normal variances and the difference in asymptote for the streamwise variances is caused by the high free-stream tunnel noise. The shear stress plots agree in trend, but differ in numerical agreement, especially in the near-wall region. We suspect that this is the result of spatial filtering near the wall. Both shear stress plots approach zero in the freestream, so we know that even despite high freestream turbulence, the streamwise and wall-normal fluctuations are uncorrelated an therefore do not contribute to production of turbulent kinetic energy. The underlying turbulent boundary layer should be relatively unaffected.

Figure 4.6 shows the fluctuation velocity variances and turbulent shear stresses for the current case C, and the current + wave cases W1C and W2C. When waves are introduced, we notice a peak in the streamwise velocity fluctuation variances at $y/\delta_o = 1.5$, which appears to increase with wave strength. Moreover, the location of the peak appears to coincide with an inflection in turbulent shear stress gradient. In order to determine whether this peak is significant, we aim to verify its validity since its existence does not appear to have been discussed in prior literature. We start by looking at the phase dependence of this phenomenon. We start by considering the subset of frames of common phase. The streamwise fluctuations at each wall-normal position are calculated for each of these subsets. The results of each of the four subsets are plotted alongside the measured fluctuation variances for the entire dataset. The result is shown in Figure 4.7, which shows that the phase-segregated streamwise velocity fluctuation variances overlap with those of the entire dataset, suggesting that the observed peak is phase-insensitive. We further verify that the peak is not the result

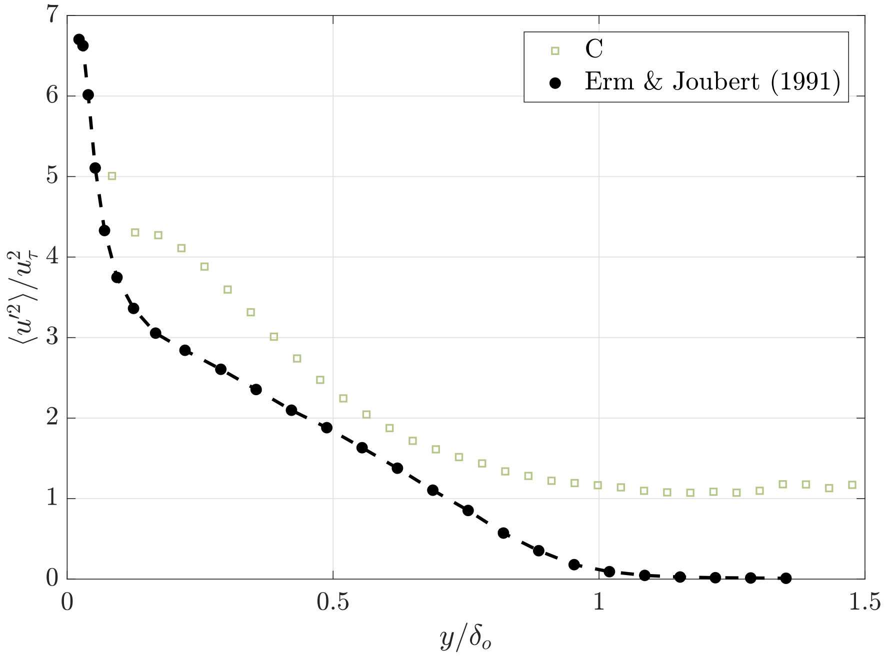

Figure 4.3: Comparison of streamwise fluctuation variances to Erm & Joubert (1991). Data sets show fairly good agreement with each other, but approach different asymptotic values in the free stream.

of a sampling error. To this end, we obtain a subset of 2,000 randomly-sampled frames and calculate the streamwise fluctuating velocity variances on this dataset. This is repeated four times, and is compared to the streamwise velocity fluctuation variances from the full dataset. The result is shown in Figure 4.8, in which all four subsets overlap with the full dataset. Much like the phase dependence check described above, the streamwise velocity fluctuation variances from all four subsets of random frames overlap with those from the full dataset, suggesting that the peak is not the result of a sampling error.

4.3 Summary

One of the goals of point-wise statistical methods is to establish agreement with previous experiments, so as to validate our observations when we examine the resulting POD modes in

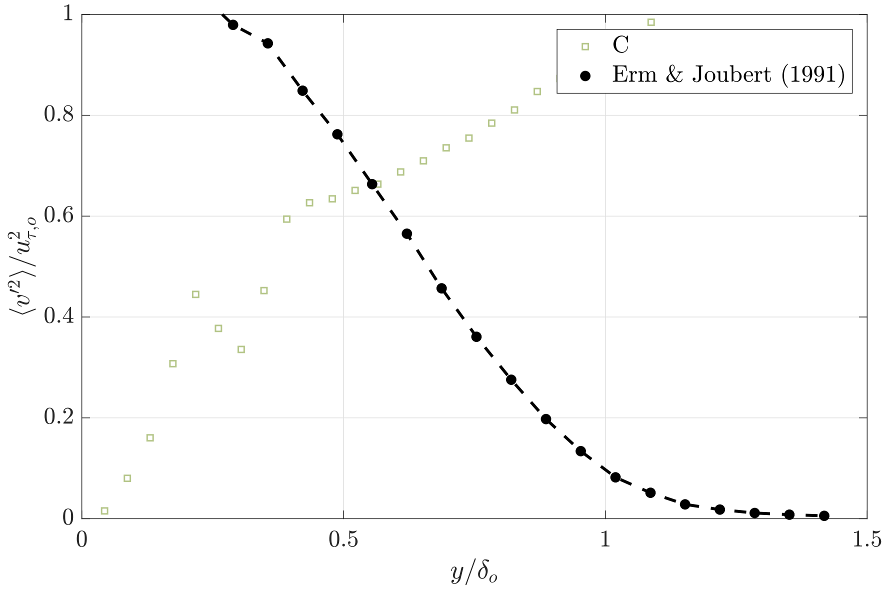

Figure 4.4: Comparison of wall-normal fluctuation variances to Erm & Joubert (1991). Current-only data suggests that high freestream turbulence contributes to the disagreement between experimental datasets.

Chapter 5. In this experiment, we establish relatively good agreement in mean velocity profile with Kemp & Simons (1982) and Klopman (1994), in that the mean velocity gradient at the wall appears higher near the wall. Streamwise velocity fluctuations in wave-free cases roughly correspond to profiles observed in Erm & Joubert (1991). The changes in sign of $\langle u'v' \rangle$ when a wave-turbulent boundary layer interaction exists, as observed in Umeyama (2005), are also repeated in this experiment. Additionally, we note the existence of a peak in these fluctuations at $y/\delta_o = 1.5$ which becomes more prominent with increasing wave amplitude. Despite this, poor agreement exists between wall-normal velocity variances between this experiment and in Erm & Joubert (1991), perhaps due to the high freestream turbulence.

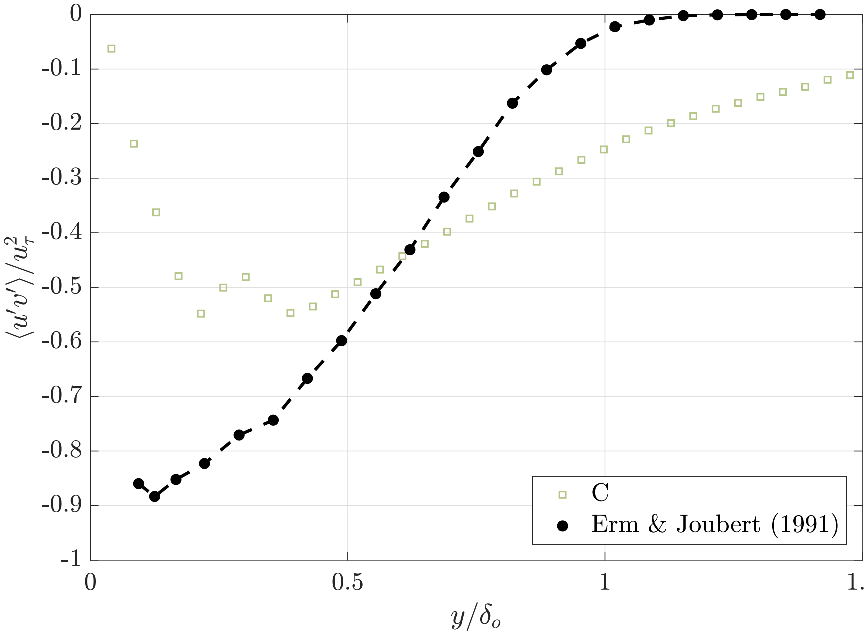

Figure 4.5: Comparison of Reynolds shear stresses to Erm & Joubert (1991). Current-only data from this experiment resembles the shape of what is provided in Erm & Joubert, but suggests a larger δ_o value than what is calculated using statistics from the mean streamwise velocity profile.

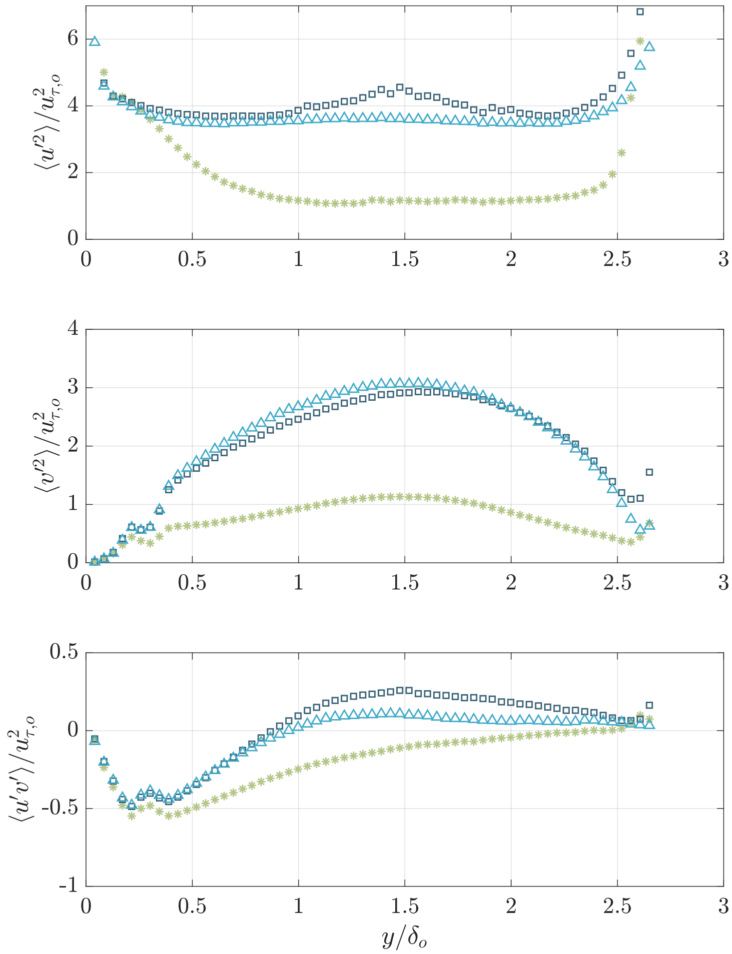

Figure 4.6: Velocity fluctuation variances of the streamwise, wall-normal, and shear components. Data suggests a peak in streamwise fluctuation variance (top), corresponding with a change in sign of the shear velocity (bottom) gradient, at $y/\delta_o = 1.5$ when the turbulent boundary layer is perturbed with a surface wave. An abnormality exists in wall-normal velocity variance near the wall, which we suspect is the result of wall reflections.

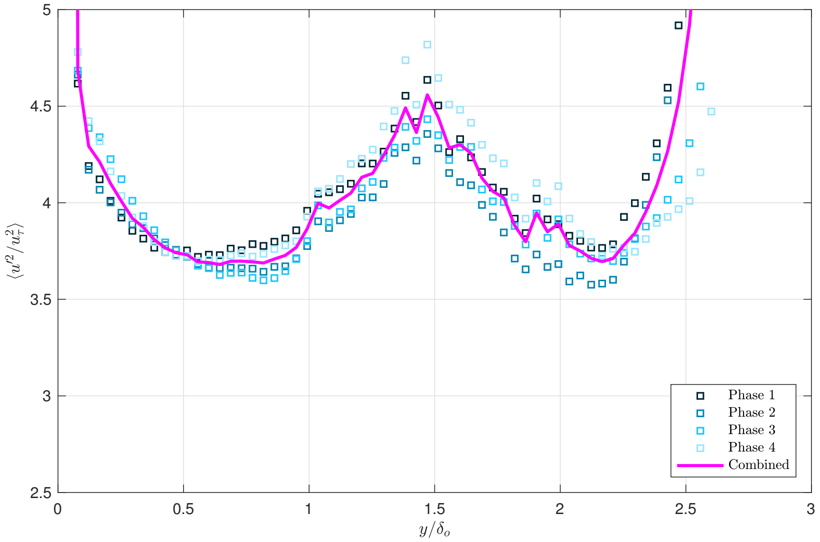

Figure 4.7: Graph of the phase-segregated $\langle u'^2\rangle/u_\tau^2$ in W2C and the combined result using all frames. The overlapping plots suggest that the peak is phase-insensitive.

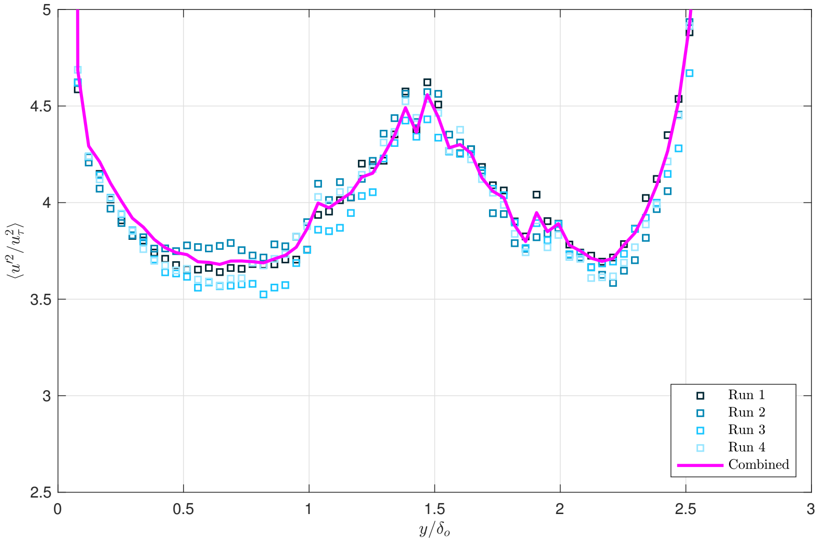

Figure 4.8: Graph of the $\langle u'^2\rangle/u_\tau^2$ for a subset of 2000 randomly selected frames in W2C and the combined result using all frames. The overlapping plots suggest that the peak is not the result of a sampling error.

Chapter 5

PROPER ORTHOGONAL DECOMPOSITION

5.1 Introduction to POD

Proper orthogonal decomposition (POD) is a subset of Principal Component Analysis (PCA), where the kernel takes the form of a squared velocity. In turbulent flow, it has been shown to be a powerful tool in the identification of features present in a turbulent boundary layer. POD minimizes the co-variances in the correlation tensor, producing a set of orthogonal modes which can be used for analysis. In our analysis of the turbulent boundary layer, we perform POD on the streamwise fluctuating velocity u'. This means that the resulting modes are weighted by their contributions to streamwise kinetic energy u'^2, and that the resulting spatial modes are in u', and can therefore be useful in analyzing turbulent production as shown in a Reynolds decomposition of the Navier-Stokes equations. Mathematically, POD returns modes such that

$$u(\mathbf{x}, t) = \sum_{n=1}^{N} a(t)\phi(\mathbf{x})$$

where $\phi(\mathbf{x})$ are the resulting spatial modes and $a(t)$ is a time-varying coefficient.

POD has been helpful in interpreting the spatial structure of turbulent flows which was previously impossible with point-wise statistical information. Previous results discussed in Chapter 1 showed significant changes to the mean velocity profile of the turbulent boundary layer when subjected to surface waves. These results suggested that the interaction is non-linear, and that the changes to the underlying turbulence structure were the result of the presence of waves. We also indicated that it would be difficult to characterize using point-wise statistical methods.

Alternatively, POD is able to decompose the turbulent boundary layer into its constituent modes. These modes minimize the off-diagonal terms of the $u'_1 u'_2$ covariance matrix; that is, they are the most optimal set of modes that can describe the flow. Any frame can be reconstructed as a linear combination of these modes, analogous to how the modes of vibration can be used to reconstruct the vibration of a beam. In analyzing these constituent modes, we are thus able to observe the spatial characteristics of the flow, and to identify changes in these structures when subjected for forcing. Previous experiments employing POD have been successful in identifying constituent structures in turbulent flow, such as the identification and reconstruction of the very-large-scale motions (VLSMs) in turbulent pipe flow (Hellström, 2011, Figure 5.1). In this experiment, we expect to identify a number of identifying features of the turbulent boundary layer structure using POD.

To efficiently produce highly converged modes in a turbulent flow with a wide range of length scales, a large amount of data is required. Conventional POD would produce a number of modes equal to the number of frames used in the calculation. As we are only concerned with the largest, most energetic structures, it would be much more computationally efficient to calculated only these modes instead of the full set. As such, we employ randomized sampling POD (Halko et. al. 2009). This method approximates the spatial modes using a randomized sampling technique without the need to compute the full POD. For large datasets such as ours, computing the full POD is both time-and resource-intensive, requires an inversion of an astronomically large matrix, and calculates extraneous, low-energy modes that are known to be spatially filtered. The randomized-sampling method allows us to specify the number of modes needed, and is able to converge these lower-order modes given a sufficient amount of data using a method that is considerably less resource- and time-intensive. In this experiment, we converge only the first 1,000 modes (out of a theoretical total of 20,000 modes) since we expect that the first few converged modes characterize these inclined, attached structures of interest.

5.2 Snapshot POD & the Turbulent Boundary Layer

In channel flow, a POD decomposition reveals alternating, high/low streamwise momentum structures which are attached to the wall and are inclined in the direction of the flow, as

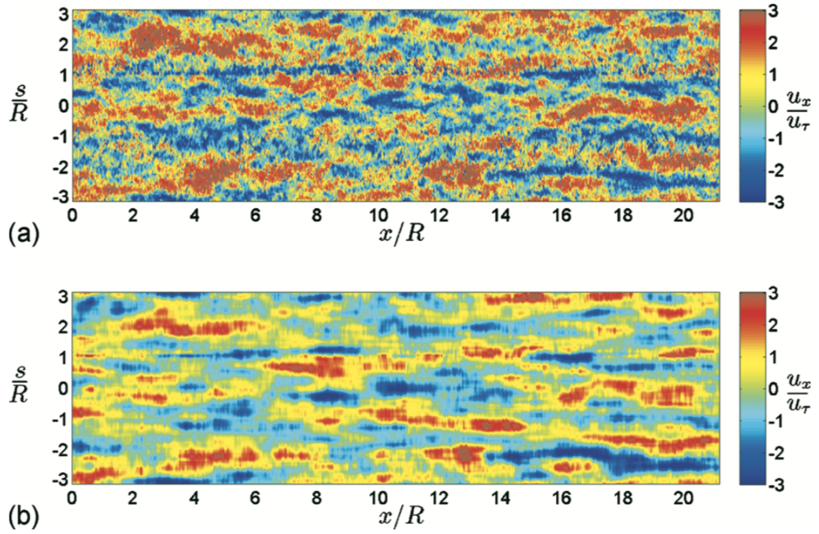

Figure 5.1: Streamwise velocity fluctuations from turbulent pipe flow (top) and a reconstruction using the 10 more energetic POD modes. Taken from Hellström (2011)

shown in Williams (2017, Figure 5.2), where wind tunnel flow was used to capture data. These alternating momentum structures, reminiscent of hairpin packets, have corresponding wall-normal momentum modes that appear opposite in sign and are therefore regions of negative shear stresses. The turbulent kinetic energy equation tells us that the dominant production term is

$$\mathcal{P} = -\rho\langle u'v'\rangle\frac{\partial\bar{u}}{\partial y}$$

where $\partial\bar{u}/\partial y$ is the mean velocity gradient (usually positive in the turbulent boundary layer), and $\langle u'v'\rangle$ is the Reynolds stress. Therefore, when the mean streamwise and wall-normal fluctuations are anti-correlated, they result in production of turbulent kinetic energy. A set of modes from the current-only case C is plotted in Figures 5.3 and 5.4. POD is performed on a subregion where $0 < y < \delta_o$, for reasons which are explained in the next section. The modes are plotted from lowest order to highest order, weighted such that lower-order modes contribute most to turbulent kinetic energy. Red regions denote areas of positive fluctuating velocity, and blue regions denote areas of negative fluctuating velocity. Each mode is

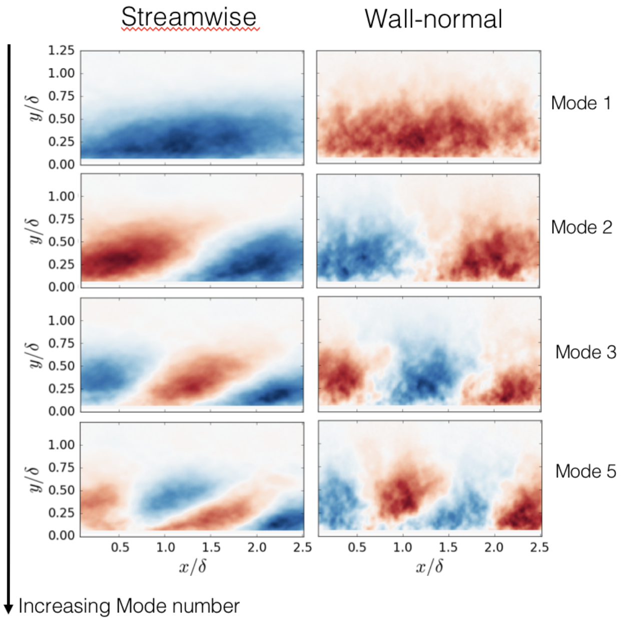

Figure 5.2: Streamwise (left) and wall-normal (right) modes obtained using PIV data from wind tunnel experiments (Williams 2017, data processed after publication). Positive streamwise momentum regions correspond to negative wall-normal momentum regions (and vice versa), resulting in high shear stress and turbulent production.

normalized by the maximum absolute value in the mode. The left column shows streamwise fluctuating velocity modes, and the middle column shows wall-normal fluctuating velocity modes. The right column represents the shear stresses, which is calculated by a point-wise multiplication of the streamwise and wall-normal fluctuating velocity modes. The outlined structures detail what we are interested in: namely, the wall-attached, inclined structures. These are the structures which are typically anti-correlated and therefore contribute to turbulent kinetic energy. Note how, in streamwise mode 6 for example, the positive streamwise fluctuating velocity regions inside the yellow outline correspond to negative fluctuating velocity regions in the wall-normal mode. The point-wise multiplication reveals regions of high negative shear stress, and thus positive production. This phenomenon can also be seen in modes 4 and 9.

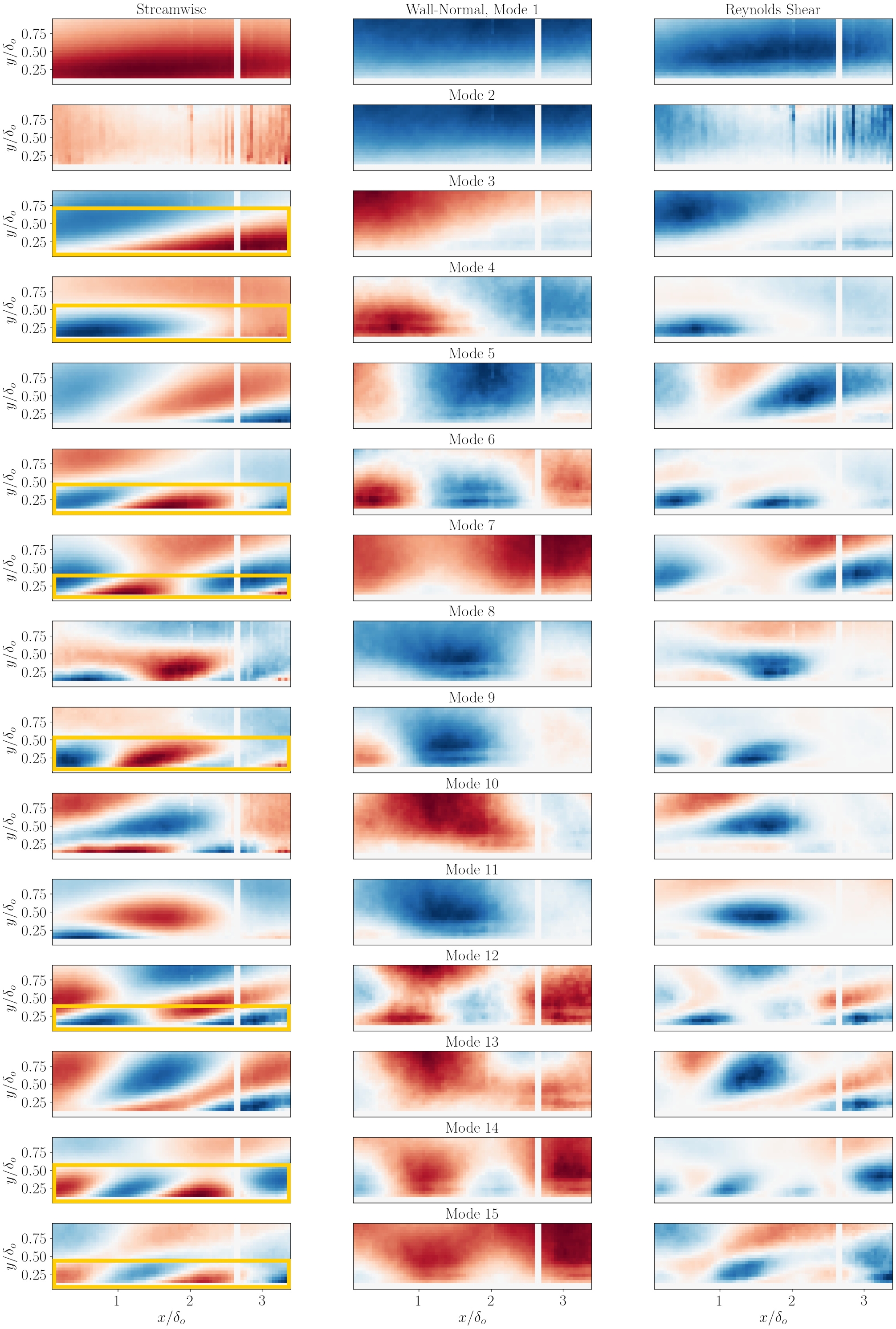

Figure 5.3: Modes 1-15 of the fluctuating velocities for the current-only case C. Regions representing the attached, inclined structures are highlighted in yellow.

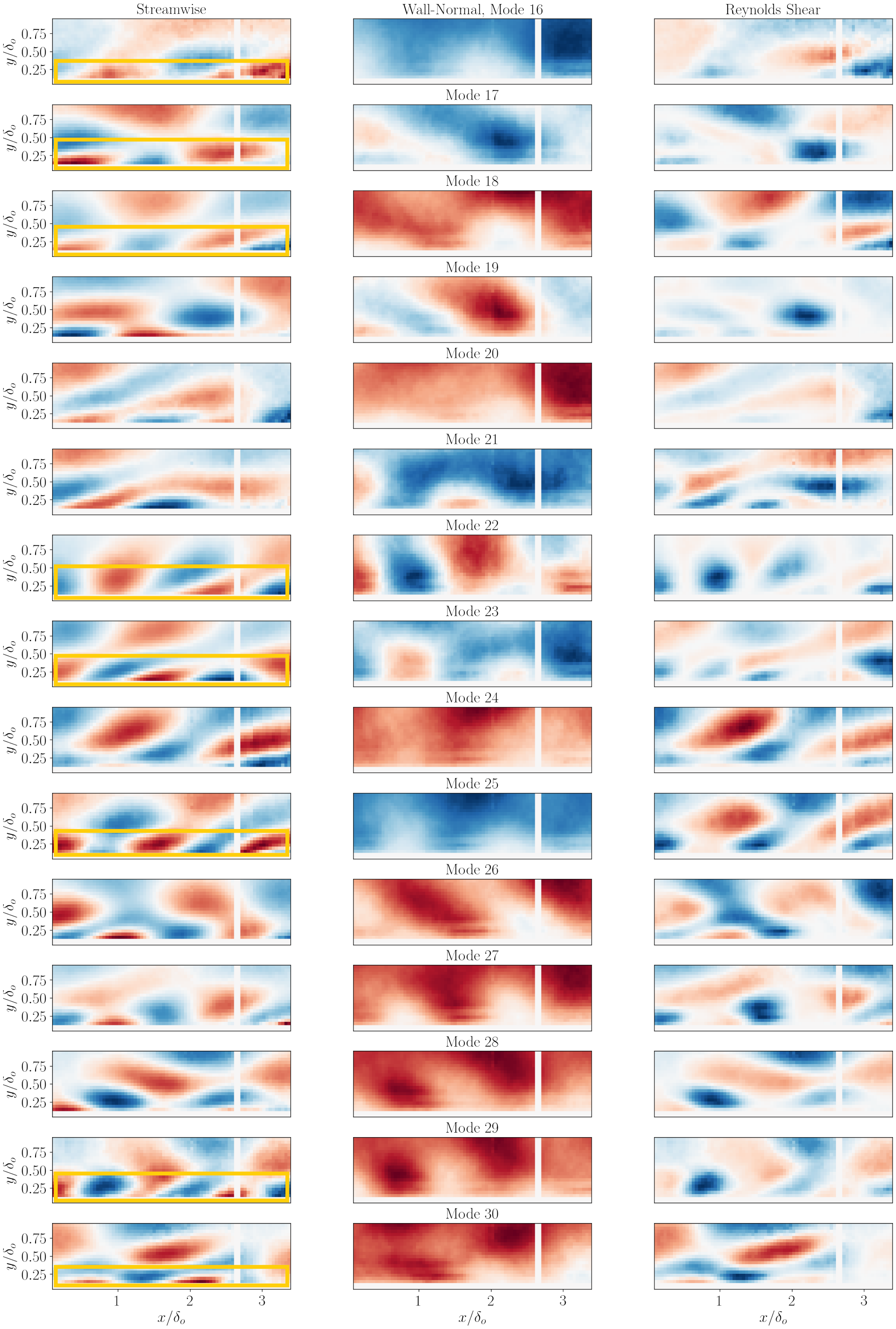

Figure 5.4: Modes 16-30 of the fluctuating velocities for the current-only case C. Regions representing the attached, inclined structures are highlighted in yellow.

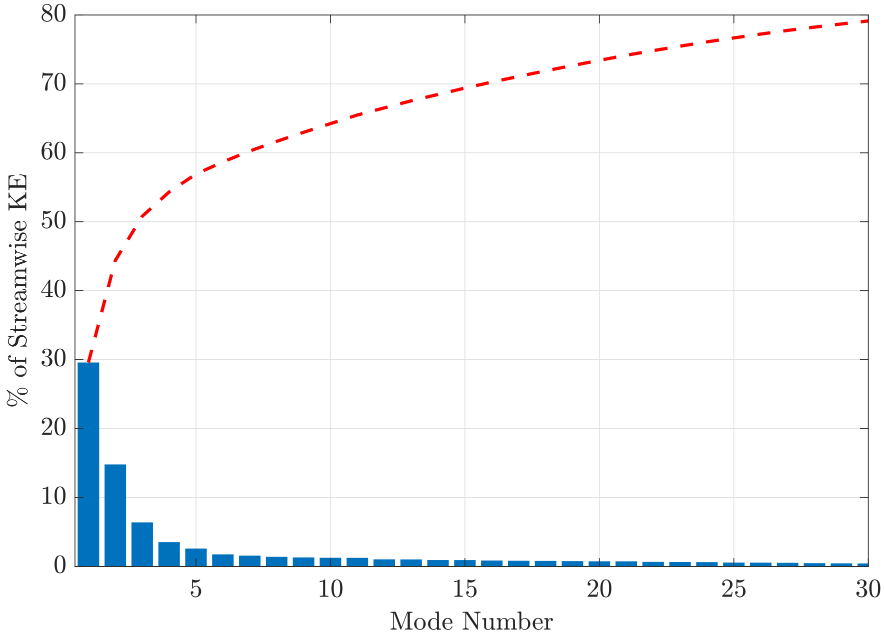

Figure 5.5: Mode energy spectrum for the first 30 modes of the current-only case C. The red dashed line denotes the integrated energy contained.

The relative turbulent kinetic energy contained in each mode is shown in Figure 5.5. From the modal energy set, we see that the first mode (the lowest-order mode) contains roughly 30% of the total streamwise turbulent kinetic energy, and that the spectrum becomes more and more uniform with increasing mode number. Note how the integrated energy increases rapidly such that the first 30 modes contain roughly 80% of the total turbulent kinetic energy. Higher-order modes do not merit as much consideration beyond the 30-mode threshold for two reasons: first, a minority of the energy total (roughly 20%) is distributed among the remaining 970 modes. Second, the structures in these modes tend to be small, and are spatially filtered by the camera.

5.3 POD Noise Sensitivity

Freestream turbulence significantly affects v', as described earlier. This raises concerns of whether the wall-normal modes may reflect unexpected structures other than the attached, inclined ones of interest. Figure 5.6 shows the streamwise POD modes calculated using both u' and v' in the left column, and just u' in the right column. Green arrows show corresponding modes between the POD applications on u' and v', and on u' alone. The POD on both u' and v' reveals extraneous modes which do not correspond to the attached, inclined structures of interest in this experiment. These extraneous modes, with structures outside of the boundary layer, do not appear in the POD performed solely on u', leading us to believe that there are structures (or perhaps noise) in v' which do not correspond to the attached, inclined modes of interest. This problem is mitigated by performing a POD on u' alone, and we reconstruct the v' modes using a reconstruction method. Indeed, the modes seen in Figure 5.3 and 5.4 were calculated using this reconstruction method, discussed next.

To reconstruct the v' modes, we first calculate the activation of each streamwise mode on the streamwise velocity part of each frame in the dataset (20,000 in all). This is accomplished by calculating the projection of each streamwise frame on each streamwise mode. The wall-normal mode is then constructed as the summation of the corresponding wall-normal frames, weighted by their streamwise activations of the particular mode in each frame. This produces roughly the same wall-normal modes as the POD including both u' and v', while removing extraneous modes that are influenced more heavily by wall-normal motions. The formal and reconstruction methods differ in kinetic energy distribution because the reconstruction method accounts only for u^2 – the kinetic energy in the streamwise direction.

A POD on the boundary layer only $y < \delta_o$ and using the reconstruction method appears to produce even better results since turbulent motions near the free surface are excluded. The case discussed in the previous section, using Figures 5.3 and 5.4, shows that nearly all of the lower-order streamwise modes identified can be associated with the wall-attached, inclined modes of interest. Therefore, all of the POD analyses performed in this experiment considers only the boundary layer ($y < \delta_o$) to obtain u' modes, and uses a reconstruction method to obtain the v' modes.

5.4 Modal Convergence

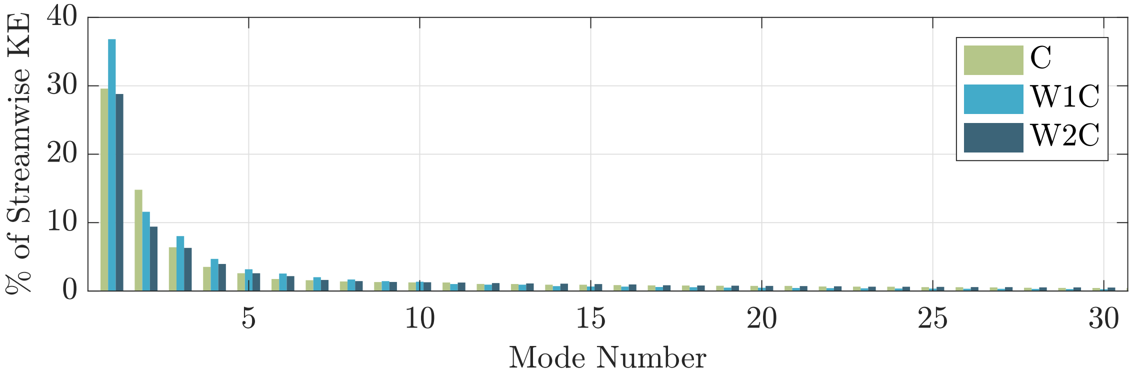

Figure 5.7: Energy spectrum for C, W1C, and W2C.

Figure 5.8 shows a comparison of the calculated streamwise POD modes for the full set of data (20,000 frames, left) and the calculated streamwise POD modes using a subset of the dataset (15,000 frames, right), both for the current-only case C. The 10 modes of lowest order, accounting for roughly 60% of the streamwise kinetic energy, are plotted in this figure. Between the two subsets, we see only slight changes in the modal structure. There are some changes in mode order between the two cases; however, these changes in order occur at higher-order modes, where the energy distribution is more uniform. Thus even slight changes in the modal energies calculated between the cases can cause changes to the mode order, and as such, a small change in order is a minimal difference between the two cases. From an analysis of the high-order modes, we note reasonable convergence up to streamwise mode 30. Thus we can conclude that the modes obtained using 20,000 frames are converged up to 30 modes.

It should be noted that, in this comparison as well as all of our POD analyses, we do not distinguish modes by changes in sign. An example is mode 4 in Figure 5.8. This is because the activation a_n of each mode is calculated by the projection of the mode onto each frame, which can be either positive or negative.

5.5 Modal Analysis, Current-only case (C)

Figures 5.3 and 5.4, as discussed previously, show the first 30 modes of the current-only case C. Streamwise modes were computed directly using Snapshot POD, and wall-normal modes were reconstructed using the method described in Section 5.3. Streamwise modes showing the expected attached, inclined structures are outlined in yellow. The attached, inclined structures in the streamwise modes exhibit a moderate incline in the direction of the flow of about $8 - 15°$, which is in line with the angle of hairpin packets found in previous studies of unperturbed boundary layers (see summary of previous results in Volino et. al. 2007). Combined with the wall-normal modes, these regions produce strong negative shear stress near the wall, and suggest regions of high turbulent kinetic energy production. Modes such as 6 and 7 appear to be phase-shifted pairs of each other, suggesting that these structures convect in the streamwise direction.

There are modes present in the flow which do not exhibit the attached, inclined structures we are interested in. Examples of these modes are mode 10, 11, and 20, which may represent freestream turbulence (noise in the tunnel is $5\% u_\infty$), or they may be older structures that have detached from the wall. We are not interested in either, since these modes will be difficult to distinguish from wave effects when waves are introduced.

5.6 Modal Analysis, Current + Waves (W1C, W2C)

The first 30 modes of the waves + current case W1C are plotted in Figure 5.10 and 5.11, and the energy spectrum for this case is plotted in Figure 5.7. Wall-attached structures, similar to the inclined, attached structures identified in the current-only case C, are identified in the streamwise modes. Some examples of these structures are outlined in modes 6, 10, and 11. We note that the identified modes appear to exhibit a higher inclination compared with the current-only case C when wave forcing is introduced. Moreover, in wall-normal modes

5, 8, and 13, we note that some of the modes appear inclined in the upstream direction near the freestream. This is an interesting result as it suggests that the structures are heavily influenced by the wave-induced motions.

Throughout all mode numbers, the wall-normal modes no longer appear attached to the wall. Whereas several attached wall-normal modes can be observed in the current-only mode C (Figure 5.3, modes 4, 6, 12, and 14), only mode 12 in the wave-forced case W1C could be considered an attached mode. Instead, most wall-normal modes in case W1C appear to lie at wall-normal distances further from the boundary. As a result, regions of the most intense shear stresses now cluster further from the wall. This is a departure from the current-only case, where it was noted that the shear stresses appeared to be strongest in regions near the boundary. In addition, there are now areas of strong positive shear stresses, as shown in modes 6, 8, and 11, which potentially correspond to areas of turbulent destruction.

Figure 5.9 shows a wave mode corresponding to a wave harmonic in the absence of current. The figure shows the areas of alternating positive and negative induced streamwise and wall-normal velocities due to the presence of the surface wave. These structures are similar in shape to the detached wall-normal modes in case W1C, which suggests that the wave has a significant impact on the streamwise fluctuating velocity field. This effect is seen in wall-normal modes 4-6 and 8-10. This suggests that the wave harmonics, in some way, affect the structure of the wall-normal modes. The streamwise modes, however, are only affected by a change in the original structure such that the modes are more inclined. This uneven altering of the streamwise and wall-normal modes results in a loss of anti-correlation between regions of streamwise and wall-normal momentum, which significantly affects turbulent production.

Figures 5.12 and 5.13 show the first 30 modes for the stronger wave + current case W2C, and Figure 5.7 shows the modal energy spectrum. The first 8 modes, representing about 60% of the total streamwise turbulent kinetic energy in both wave cases W1C and W2C, are nearly identical in structure. Only after mode 9, where no mode represents more than 2% of the total kinetic energy among the first 1000 modes, do we begin to observe changes from the modes in W1C. Some of the higher-order modes remain similar between the wave cases but change in mode order. This suggests that the modal changes, at least at the largest scales, are insensitive changes in wave strength.

In conclusion, it appears that the streamwise and wall-normal modes exhibit unequal changes when subjected to surface wave forcing. Compared to the current-only case C, the streamwise modes appear more inclined. The structures in the wall-normal modes now appear further from the boundary, and in some instances, appear inclined in the upstream direction. Combined, the shear stresses are neither as negative nor as concentrated near the wall. Instead, regions of both strong positive and negative shear stresses now appear at wall-normal locations away from the wall, as seen in modes 6 and 13. This suggests that net turbulent production is reduced within the boundary layer. It is important to note that within the boundary layer itself, the mean velocity gradient is positive. Therefore, negative shear stress events produce turbulent kinetic energy, even in regions away from the wall but within the boundary layer.

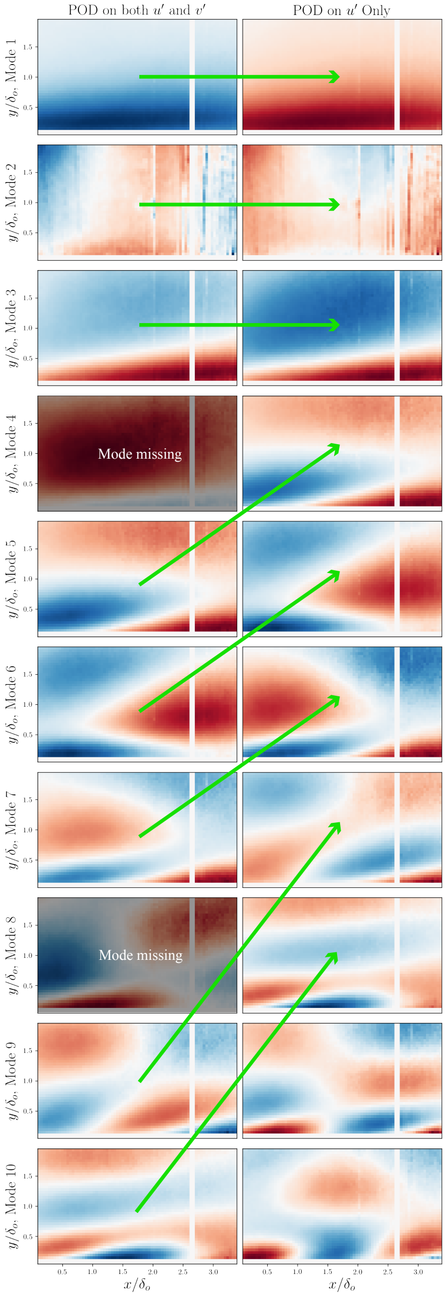

Figure 5.6: Mode comparison between POD on u' and v' and POD on u' alone. Green arrows link the corresponding modes between the two cases. Modes 4 and 8 are missing from the POD on u' only, suggesting that the mode represents unsteadiness in v'.

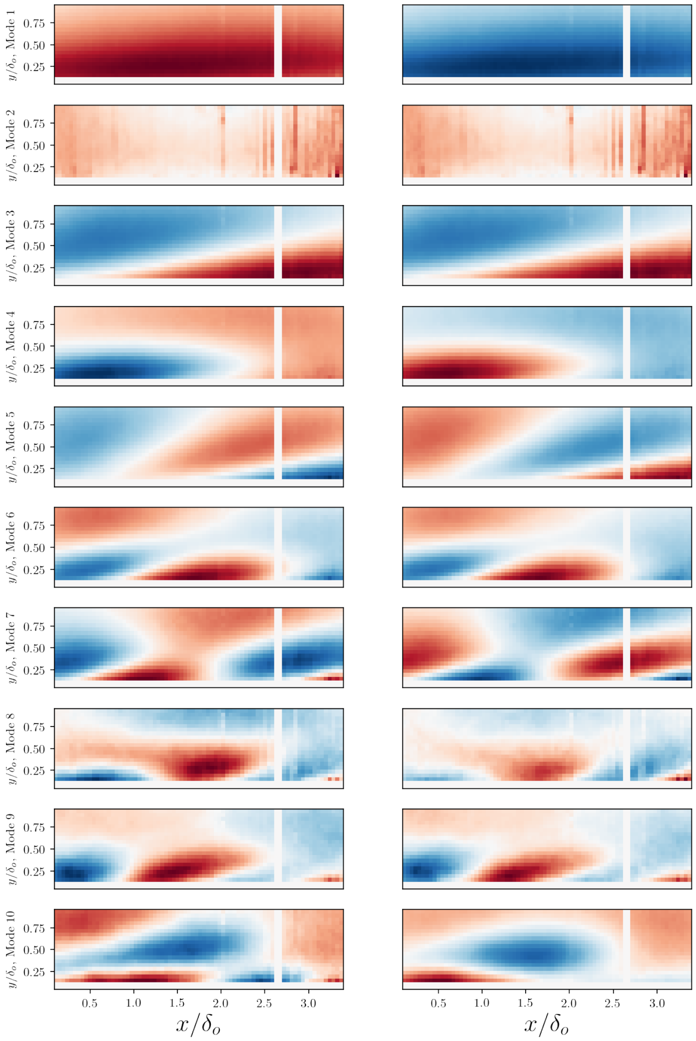

Figure 5.8: Comparison of streamwise modes between the full dataset (left) and the subset (right) for the current-only case C. The modes are similar in shape. Higher-order modes are susceptible to changes in mode order because the energy at higher-order modes is more uniform.

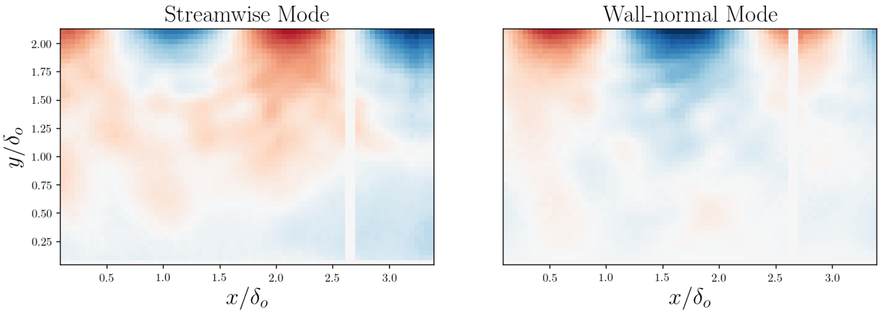

Figure 5.9: Sample POD mode (mode 6) of the W1 case. This mode is structurally similar to the wall-normal turbulent boundary layer modes when subjected to wave forcing.

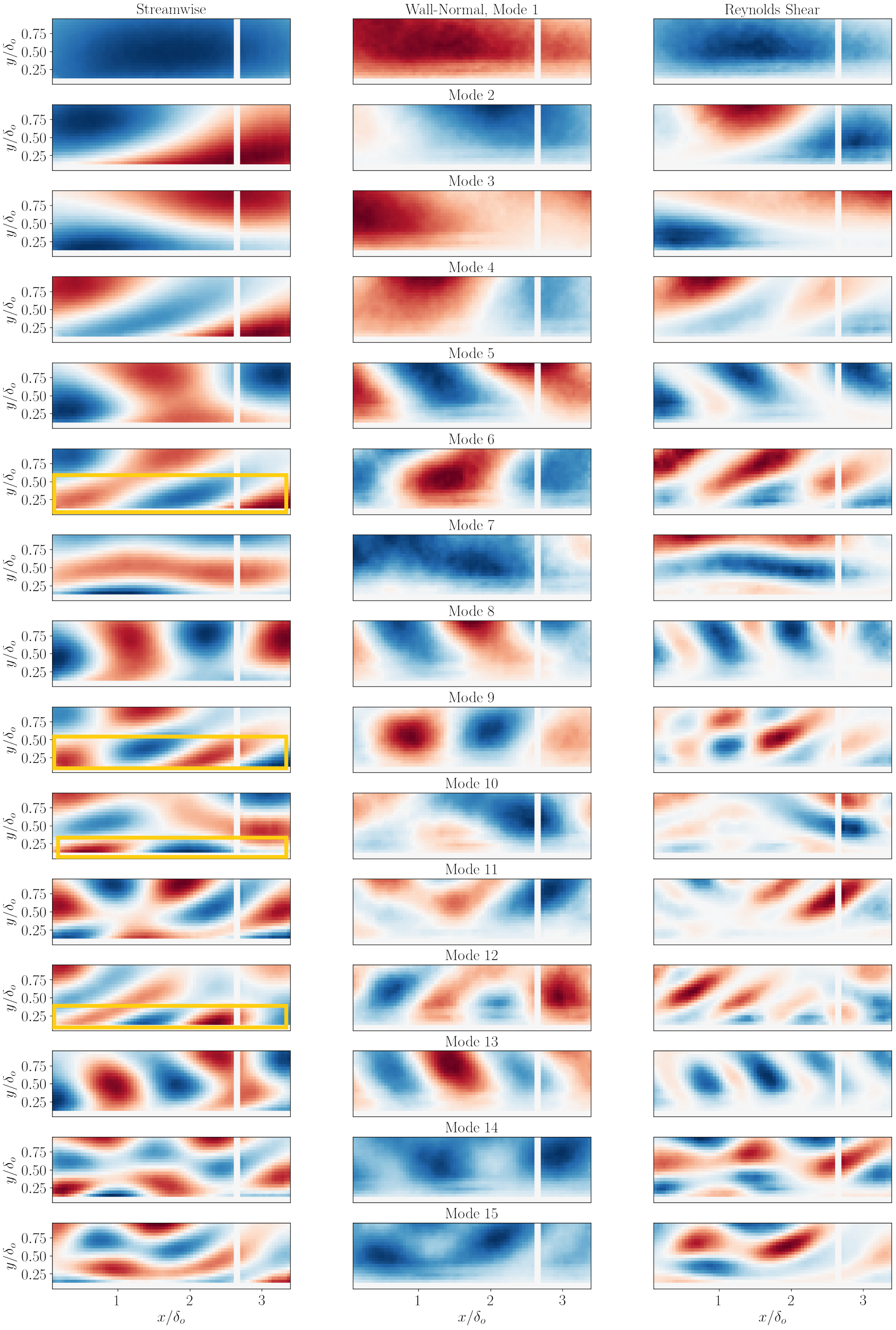

Figure 5.10: Modes 1-15 of the fluctuating velocities for the current + weak waves case W1C. Regions representing the attached, inclined structures are highlighted in yellow.

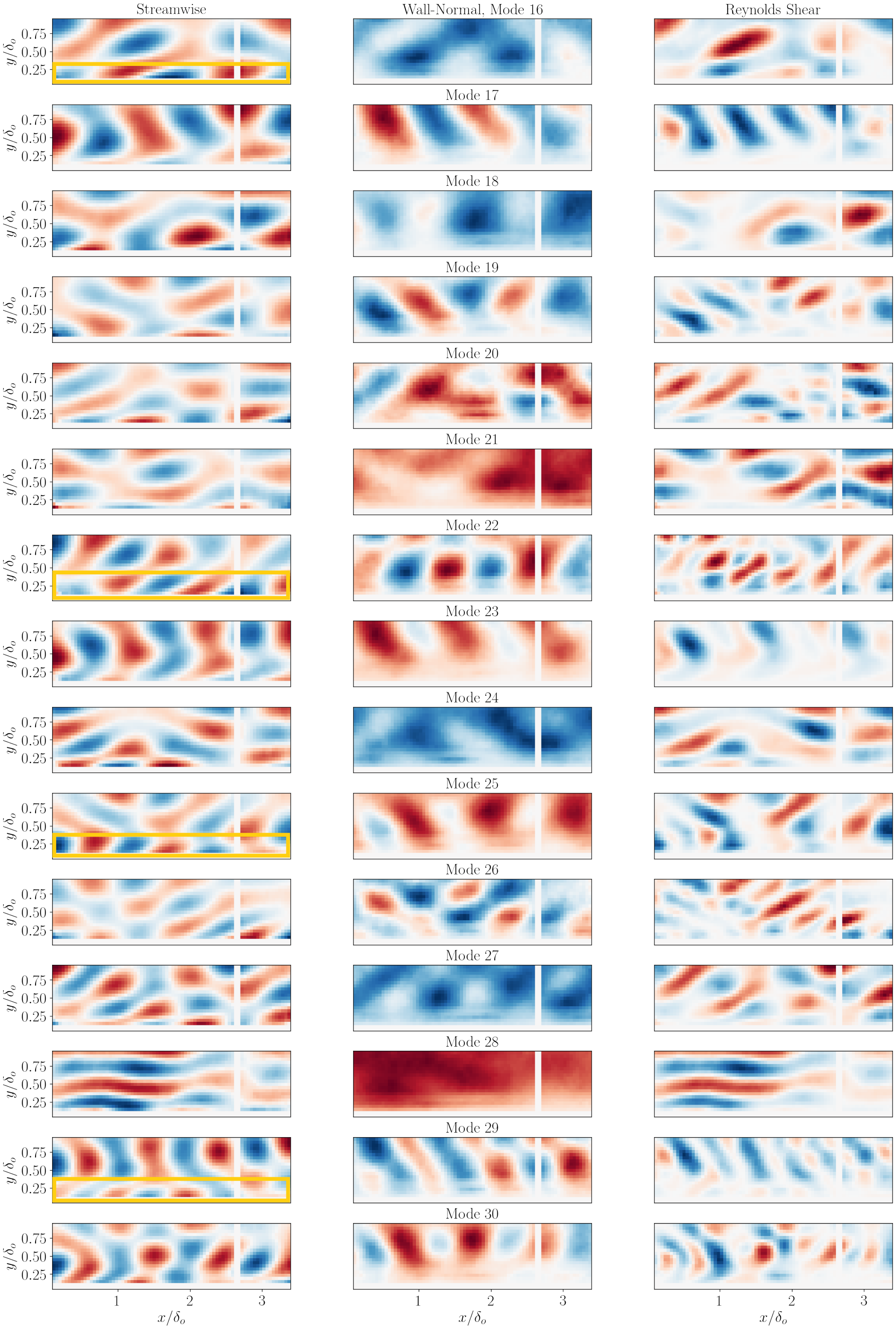

Figure 5.11: Modes 16-30 of the fluctuating velocities for the current + weak waves W1C. Regions representing the attached, inclined structures are highlighted in yellow. Note that far fewer structures can be identified, and of those, fewer represent areas of turbulent production.

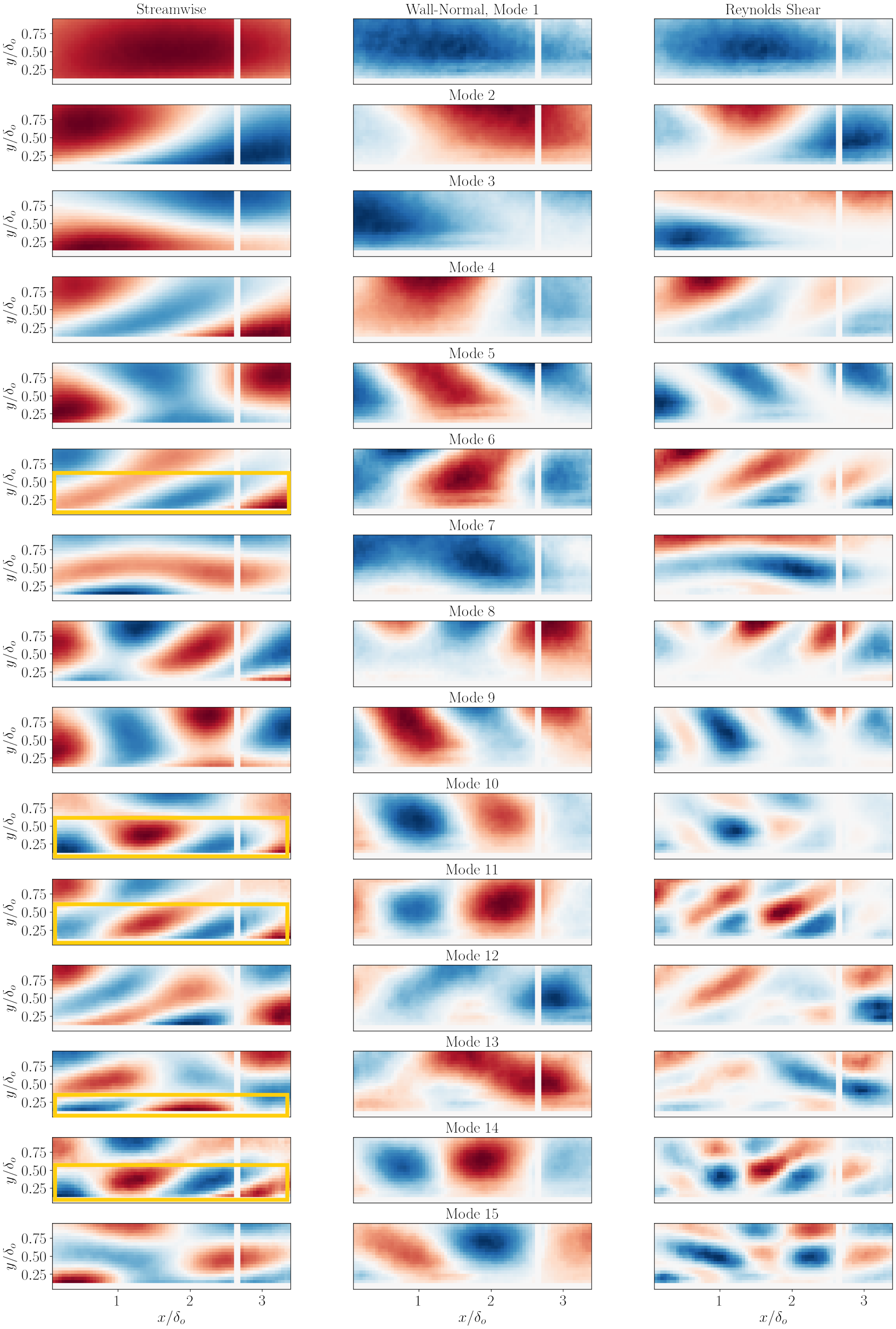

Figure 5.12: Modes 1-15 of the fluctuating velocities for the current + weak waves case W2C. Regions representing the attached, inclined structures are highlighted in yellow. Note that far fewer structures can be identified, and of those, fewer represent areas of turbulent production.

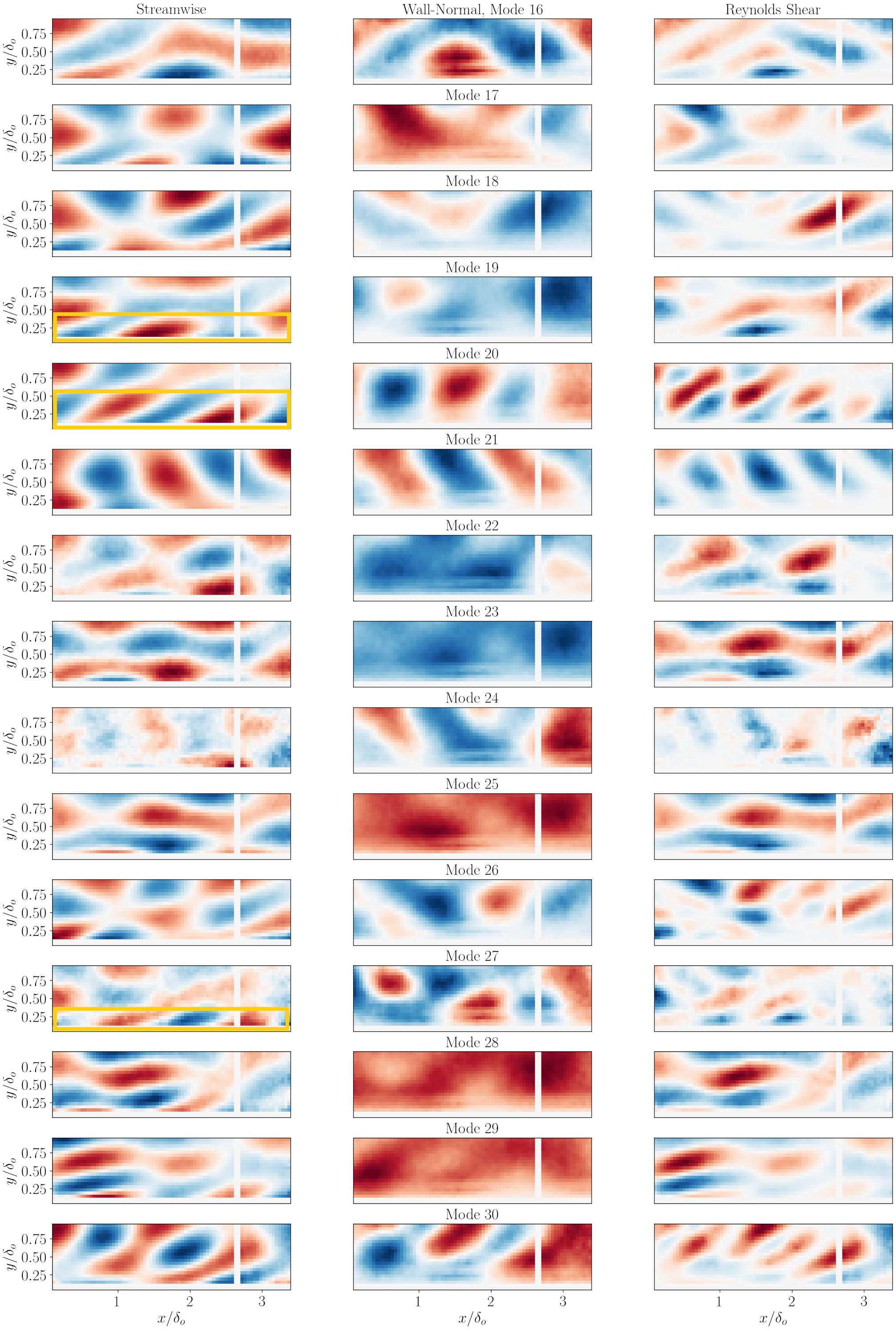

Figure 5.13: Modes 16-30 of the fluctuating velocities for the current + weak waves W2C. Regions representing the attached, inclined structures are highlighted in yellow. Note that far fewer structures can be identified, and of those, fewer represent areas of turbulent production.

Chapter 6

CONCLUSION

Turbulent boundary layer data collected at the Washington Air-Sea Interaction Research Facility (WASIRF) is analyzed using statistical point-wise methods and proper orthogonal decomposition. In the current-only case, profiles in streamwise velocity fluctuation variance $\langle u'^2 \rangle$ and in turbulent shear $\langle u'v' \rangle$ follow the expected trends from previous experiments. Wall-normal velocity variances do not agree with previous experiments, which we believe is an effect of high free-stream turbulence ($5\% u_\infty$).

A peak in streamwise velocity variance $\langle u'^2 \rangle$ appears when the turbulent boundary layer is subjected to surface waves. This peak appears at $y/\delta_o = 1.5$ and appears to become more prominent with increasing wave strength. The location of peak corresponds to maximum positive turbulent shear stress.

Streamwise POD modes were computed directly. Wall-normal modes were reconstructed by computing an average of the corresponding streamwise frames, weighted by the activation of the streamwise modes on each streamwise frame. This was done to minimize the effect of freestream turbulence on the POD modes. Even despite freestream turbulence of about $5\% u_\infty$, attached inclined near-wall structures that contribute to negative shear stress could still be identified using POD. The streamwise modes show that the near-wall structures exhibit a modest incline $8-15^\circ$, consistent with the inclination of hairpin packets (see summary of previous results in Volino et. al. 2007). The streamwise and wall-normal structures near the wall are also anti-correlated. Combined with a positive mean velocity gradient, these regions of negative shear stress contribute to turbulent kinetic energy production.

When surface wave forcing is introduced, widespread changes occur in both the streamwise and wall-normal modes. The streamwise modes appear more inclined relative to the free-stream, and the wall-normal modes no longer appear attached to the wall. These wall-normal modes also appear in alternating high-low momentum regions in a pattern consistent with wave-induced motion, but with a streamwise lengthscale that does not correspond to that of a surface wave harmonic. In a number of wall-normal modes, these patterns are inclined in the upstream direction. These changes in both the streamwise and wall-normal modes indicate a weakening of the turbulent production by the attached, near-wall structures. Increased positive shear events now occur away from the wall. Overall, these results indicate strong changes in turbulent structure due to the presence of surface waves, with wall-normal motions more greatly affected than those in the streamwise direction, causing significant changes in the shear stresses present in the turbulent boundary layer.

BIBLIOGRAPHY

[1] Adrian, R.J., Meinhart, C.D., Tomkins, C.D. Vortex organization in the outer region of the turbulent boundary layer. *Journal of Fluid Mechanics* **422** (2000) pp 1-54.

[2] Dean, R.G., Dalrymple, R.A. Water Wave Mechanics for Engineers & Scientists. World Scientific Publishing Company (1984) pp. 38-45.

[3] Erm, L., Joubert, P. Low-Reynolds-number turbulent boundary layers. *Journal of Fluid Mechanics* **230** (1991) pp. 1-44.

[4] Halko, N., Martinsson, P.G., Tropp, J.A. Finding structure with randomness: Stochastic algorithms for constructing approximate matrix decompositions. arXiv: 0909.4061.

[5] Hellström, L.H., Sinha, A., Smits, A.J. Visualizing the very-large-scale motions in turbulent pipe flow. *Physics of Fluids* **23**.

[6] Hellström, L.H., Smits, A.J. The energetic motions in turbulent pipe flow. *Physics of Fluids* **26** (2014).

[7] Hellström, L.H., Marusic, I., Smits, A.J. Self-similarity of the large-scale motions in turbulent pipe flow. *Journal of Fluid Mechanics* **792** (2015) pp. 779, 701-715.

[8] Huang, N.E., Long, S.R. An experimental study of the surface elevation probability distribution and statistics of wind generated waves. *Journal of Fluid Mechanics* **101** (1980) pp. 179-200.

[9] Hussain, A., Reynolds, W. The mechanics of an organized wave in turbulent shear flow. *Journal of Fluid Mechanics* **41** (1970) pp. 241-258.

[10] Kemp, P., Simons, R. The interaction between waves and a turbulent current: waves propagating with the current. *Journal of Fluid Mechanics* **130** (1982) pp. 73-89.

[11] Klopman, G. Vertical structure of the flow due to waves and currents - Laser-doppler flow measurements for waves following or opposing a current. *Delft Hydraulics* Report H840.30 Part I.

[12] Sirovich, L. Turbulence and the dynamics of coherent structures. part 1: Coherent structures. *Quarterly of Applied Mathematics* **45** pp. 353-375.

[13] Thielicke, W., Stamhuis, E., 2014. PIVlab - time-resolved digital particle image velocimetry tool for MATLAB (version: 1.41). http://dx.doi.org/10.6084/m9.figshare.1092508.

[14] Umeyama, M. Reynolds stresses and velocity distributions in a wave-current coexisting environment. *Journal of Waterway, Port, Coastal, and Ocean Engineering* **131** (5) pp. 203-212.

[15] Volino, R.J., Schultz. M.P., Flack, K.A. Turbulence structure in rough- and smooth-wall boundary layers. *Journal of Fluid Mechanics* **592** (2007) pp. 263-293.

[16] Westerweel, J., Scarano, F. Universal outlier detection for PIV data. *Experiments in Fluids* **39** (6), pp. 1096-1100.

[17] Williams, O., Hohman, T., Van Buren, T., Bou-Zeid, E., Smits, A.J. The effect of stable thermal stratification on turbulent boundary layer statistics. *Journal of Fluid Mechanics* **812** (2017) pp. 1039-1075.

[18] Yang, S.-Q., Tan, S.-K., Lim, S.-Y. Velocity distribution and dip phenomenon in smooth uniform open channel flows. *Journal of Hydraulic Engineering* **130** (12) pp. 1179-1186.

Appendix A

WAVE SURVEY RESULTS

Waves were generated in the facility by use of a motor attached to a paddle upstream. Before the experiment was conducted, extensive testing was completed to determine possible set of wave lengths and amplitudes in various different current environments. The wave testing results are listed below. For all cases, the water depth H is 23 cm. Wave heights are measured at a distance approximately 2 m downstream from the leading edge of the plate.

A (cm)	f_{wave} (Hz)	u_∞ (m/s)	a (cm)	λ (cm)	c_{wave} (cm/s)	Notes
1	1.5	0.9	0.96	223.9	335.8	Used in experiment
2	1.5	0.9	1.90	220.1	330.2	
3	1.5	0.9	2.36	185.5	278.2	Used in experiment
4	1.5	0.9	2.61	168.9	253.3	
5	1.5	0.9	2.67	157.3	236.0	
10	1.0	0.45	3.67	137.7	91.9	Strange backflow phenomenon
10	1.5	0.45	2.82	190.4	190.4	Strange backflow phenomenon
10	1.5	0.9	2.84	213.2	319.8	
1	1.5	0	1.11	57.1	85.6	Used in experiment
1.8	1.5	0	2.18	59.4	89.0	Used in experiment
2	1.5	0	1.64	63.6	95.3	Does not follow expected trend
3	1.5	0	2.21	71.8	107.7	
5	1.5	0	4.72	38.2	58.8	
10	1.5	0	5.32	30.4	45.6	

Table A.1: Various wave cases tested with differing current speeds and motor travel distances. Data shows that as current increases, wavelength and wave speed increase, and amplitude decreases.

The trends shown in the table show that for a given paddle travel A, the amplitude a decreases, and the wavelength and wave speed increase with increasing current speed.